Residual Stresses and Thermal Expansion of Ti6Al4V Fabricated by Laser Powder Bed Fusion

McGill

Department of Mining and Materials Engineering
McGill University, Montreal, Quebec

Jason Danovitch

March 2018

A thesis submitted to McGill University in partial fulfillment of the requirements needed to obtain a Master of Engineering from the Department of Mining and Materials Engineering.

Abstract

Laser powder bed fusion (LPBF) of Ti6Al4V has become the subject of considerable attention in recent years in a variety of disciplines, notably those of the aerospace and biomedical domains. In either case, Ti6Al4V is an extremely high importance alloy due to its light weight and formidable mechanical and physical properties. With the advent of LPBF processes, it has become possible to create highly complex components that could otherwise not be constructed by conventional means, and with little to no wasted material. In order for LPBF of this alloy to become a viable processing route however, its properties and proper functioning must be ascertained. The following work explores the thermal behavior of Ti6Al4V both during and after processing by LPBF. It is well known that laser-based melting processes produce a great deal of thermal and residual stresses. The detrimental effects of these stresses were measured for a series of samples with differing geometrical features to better understand the various design constraints to consider. In parallel, a number of dilatometric samples were extracted from a separate subset of samples with varying build orientation (*X-direction*, *Z-direction*, and 45^o) and post-processing heat treatments (stress relief, mill annealing, and HIP) for the purpose of determining the effects of these processing parameters on thermal expansion. Anisotropy of various properties arising from LPBF based on build orientation has been reported in separate studies, and is observed again here for the coefficient of thermal expansion (CTE). The heat treatment applied appeared to directly affect the severity of the observed anisotropy and is discussed within.

Résumé

La fusion par laser sur lit de poudre (de l'anglais LPBF) de Ti6Al4V est devenue récemment un sujet de grande attention dans une variété de disciplines, notamment dans celles de l'aérospatiale ainsi que de la biomédecine. Pour ces derniers, cet alliage est indispensable due à son faible poids et ses propriétés mécaniques et physiques formidables. Grâce à la LPBF, il est désormais possible de créer des pièces avec une complexité irréalisable par les moyens de fabrications conventionnels, avec très peu de gaspillage. Par contre, pour que la LPBF de cet alliage devienne un processus industriel viable, ses diverses propriétés et son bon fonctionnement doivent être vérifiés. La présente étude explore le comportement thermique de Ti6Al4V durant et suite à la fabrication par LPBF. Il est bien établi que les processus de fabrication par laser, tel la LPBF, représentent une source importante de contraintes thermiques et résiduelles. Les effets de ceux-ci ont été mesurés pour une série d'échantillons ayants de différentes géométries afin de mieux comprendre certaines contraintes de conception. En parallèle, plusieurs échantillons dilatométriques ont été extraits d'une série séparée d'échantillons ayant été construits en différentes orientations (*direction X*, *direction Z*, et à *45°*) et avec différents traitements thermiques (recuit de détente, recuit à température plus élevée, et HIP) pour pouvoir déterminer les effets de ces paramètres sur l'expansion thermique. L'anisotropie de diverses propriétés suite à la fabrication par LPBF en fonction de l'orientation a été rapportée à plusieurs reprises, et est discutée ici pour le cas du coefficient d'expansion thermique (CTE). Le niveau de traitement thermique semble avoir un lien direct avec la sévérité de l'anisotropie observée et est aussi sujet de discussion dans cette étude.

Acknowledgements

I would like to take the time (and space) to formally thank my supervisor, Professor Mathieu Brochu, for welcoming me into your group and granting me an excellent project in a field which has been garnering a tremendous amount of interest. Furthermore, I would like to thank you for taking the time to guide me into becoming a better person and a better future engineer.

What follows is a long list of those whom I must also thank for putting up with me during the course of my degree. First and foremost, the $P^2[AM]^2$ research group: my peers, my friends, some of the brightest people I have ever had the privilege of meeting, who remained faithful and above all cheerful all throughout my stay. I would like to thank Jason Milligan, Lucie Nguyen and Nejib Chekir, veterans all, who provided me with invaluable help but also experience. I would like to thank Andrew Walker, Melissa Trask, Justin Mezzetta, Rodrigo Trespalacio, and Joseph Chou, my brothers and sister in arms, for their eternal friendship and support, and for always being willing to lend a hand during this shared chapter in history. And to complete the thanks owed to the research group, I would like to thank Abhi Ghosh, Ryan Chou, Javier Arreguin, Yaoyao Ding, Jose Alberto "Beto" Muniz, Masum Tuncay, Bamidele Akinrinlola, Phil Hendrickz, Sam Rudinsky, Neslihan "Nesli" Alpay, Dany Rasmussen, Yuan Tian, Xianglong Wang, and David Walker, whom I will always remember as fondly as though you were family. Thank you to all those involved in the MANU601 project. Your expertise and advice throughout my project was truly a gift.

I extend my thanks to my friends and colleagues outside of the $P^2[AM]^2$ group, namely Marianna Uceda, Fred Voisard, Dan Marchand, Harris Nami, Sara Imbriglio, and Hyeree Park. To thank you individually for all that you have given me would yield a document longer than this thesis, and so I must simply say that I could not have made it without you.

And finally, my family, for their never ending encouragement. I would like to thank my father Dave, my inspiration to become an engineer. My mother Diane, who never once stopped believing in me (even if I sometimes forgot to call). My brothers, Steven and Ryan, pillars of unwavering support. And last but not least, my loving girlfriend Alicia Howard who was with me every step of the way. Thank you for the love and kindness you have shown me and continue to show me every day.

Preface

The present thesis work has been prepared in manuscript format. All of the work presented in the following thesis document has been approved for submission by all associated industrial partners per the CRIAQ MANU 601 agreement, and comprises two research articles intended for publication in 2018. These are presented in Chapters 4 and 5 of this thesis.

Chapter 4 is intended for publication as J. Danovitch, J. Choi, N. Chekir, J. Squire and M. Brochu. *Geometric Distortions in Ti6Al4V Fabricated by Laser Powder Bed Fusion*. 2018. I was the lead investigator and was responsible for all major areas of conception, data collection and analysis, and drafting of the manuscript with the assistance of J. Choi. N. Chekir and J. Squire oversaw the CMM data collection at Liburdi Ltd. Professor M. Brochu supervised the project and provided technical advice and access to research equipment.

Chapter 5 is intended for publication as J. Danovitch, J. Choi, J. Mezzetta, L. Nguyen, N. Chekir and M. Brochu. *Relationship between microstructure and dilatation response during thermal cycling for Ti6Al4V fabricated by laser powder bed fusion*. 2018. As with Chapter 4, I was the lead investigator, responsible for all major areas of conception, data collection and analysis, as well as drafting of the manuscript with the assistance of J. Choi. J. Mezzetta produced the original samples from which the present test pieces were derived and for prior metallographic examination. L. Nguyen assisted with initial operation and data collection using the dilatometer. N. Chekir provided assistance with analysis regarding titanium metallurgy. Professor M. Brochu supervised the project and provided technical advice and access to research equipment.

Table of Contents

List of Figures

List of Tables

Chapter 1 – Introduction

1.1. Ti6Al4V

Ti6Al4V is commonly referred to as the *workhorse* of titanium alloys due to its excellent mechanical and physical properties [1], making it an ideal alloy choice for countless distinct applications. Two notable and major domains in which Ti6Al4V is used extensively are the biomedical and aerospace disciplines. Ti6Al4V is a biocompatible titanium alloy with a high corrosion resistance and as such is widely used as a biological implant material [2]. It also has a high strength-to-weight ratio, making it especially attractive for use in both gas turbine engines and certain airframe sections where the mechanical properties of aluminium would be unsuitable [3]. For both biomedical and aerospace applications, highly complex and customizable parts are often desired, thus making Ti6Al4V a particularly important candidate for additive manufacturing.

1.2. Additive Manufacturing

Additive manufacturing (AM) is a manufacturing approach which encompasses a wide variety of techniques revolving around the *bottom-up* fabrication of 3D, net-shape products, contrary to conventional *top-down* manufacturing such as forging or casting. Stereolithography using a guided laser to solidify thin layers of UV-sensitive liquid polymer is widely regarded as the first commercial emergence of AM technology [4]. At this stage, AM was primarily used as a *rapid prototyping* technique, and not for the manufacturing of final parts [5, 6]. Today, due to the tremendous increase in attention given to this technique, a multitude of AM technologies exist either commercially or conceptually for the fabrication of plastic, ceramic, metal, and even biological components. In the case of metallic AM, a high power laser or electron beam is used to melt (or simply sinter in some cases) either a continuously fed wire [7], a coaxially fed stream of

powder particles [8], or a powder bed [9, 10]. There are several key advantages to AM, most notably the ability to create highly complex geometries which would otherwise be impossible to fabricate by conventional means, as well as a theoretically drastic reduction in the amount of wasted material.

1.3. Laser Powder Bed Fusion

Laser powder bed fusion (LPBF) techniques are a subgroup of additive manufacturing processes employing a high power laser to melt, in a layer-by-layer fashion, specific areas on a bed of metallic powder resting atop a solid metal base plate. Each layer corresponds to a cross-sectional *slice* of the desired final product. Once the specific volume of powder in a layer has been successfully fused, the base plate is lowered and a sweeper carefully spreads the following layer of powder to be melted, and so on until the final product is completed [9]. Several manufacturers have made LPBF commercially available with various operating parameters often carefully tailored to suit specific pure metals and alloys. Commonly used materials for LPBF include steels, aluminium alloys, and titanium alloys [11-13] [14]. Near full density components have been successfully demonstrated to be feasible with LPBF in recent years [15].

1.4. Objectives

The objectives of this thesis are to study certain thermal response characteristics of Ti6Al4V both during and following fabrication by LPBF and thus to help elaborate the understanding and efficacy of using this process to manufacture fully-functional components. In order for these components to function properly, they must be free of geometric distortions. These distortions have been reported in previous works and are caused by the accumulation of high values of thermal and residual stresses inherent to this process and other high energy input AM processes [10, 16,

17]. In this study, samples with *at-risk* geometric features were fabricated in order to observe the relationship between slight variations in a select set of design variables and the resulting thermal stress-induced distortions.

Furthermore, following fabrication, the allowed tolerances and operational lifetime of a given component must be carefully predicted. This is especially true for applications requiring an elevated operating temperature such as with gas turbine engines as thermal expansion will occur over a large number of cycles over the course of the component's lifetime. For this, a number of dilatometric samples were extracted from a previously studied set of samples whose characteristics are known, and were then thermally cycled. Both build orientation and post-processing heat treatment were selected as variables for this study.

1.5. Thesis Outline

The body of this thesis will be divided into 5 chapters encompassing the following:

a) (Chapter 2) A literature review providing an overview of the metallurgy of Ti6Al4V, the state of the art of the LPBF process, the results of previous studies involving residual stresses in LPBF, as well as the summary of some work undertaken for dilatometry and thermal cycling of Ti6Al4V;
b) (Chapter 3) An overview of the experimental methods employed for the current study and a description of the equipment used;
c) (Chapter 4) A first presentation of results and discussions laid out under a scientific paper to be submitted entitled "Geometric distortions in Ti6Al4V fabricated by laser powder bed fusion". In this section, results pertaining to the deformation of Ti6Al4V structures with

varying geometries caused by the thermal and residual stresses inherent to the LPBF process will be discussed;

d) (Chapter 5) A second presentation of results and discussions laid out under another scientific paper to be submitted entitled “Relationship between microstructure and dilatation response during thermal cycling for Ti6Al4V fabricated by laser powder bed fusion”. This section will provide an analysis on the microstructural and dilatation response of Ti6Al4V samples extracted from a previous set of specimens manufactured by LPBF with known properties using build orientation and post-processing heat treatment as variables;

e) (Chapter 6) A final summary of the findings from this thesis.

Chapter 2 – Literature Review

Ti6Al4V is an *alpha-beta* titanium alloy with an extremely wide range of applications and commonly found in the aerospace and biomedical fields, both of which would benefit immensely from the advantages of additive manufacturing due to the high customizability inherent to the process [1, 13, 18]. In such fields where precision and long-term functionality are of key importance, the properties of the fabricated components must meet certain very stringent requirements. Residual stresses are a known issue in laser-based additive manufacturing techniques and at high magnitudes can be associated with a number of detrimental effects such as crack formation, deformations, and reduced fatigue life [13, 19]. The following literature review will focused on providing the reader with a detailed overview of (1) the known process and design variables influencing residual stress development in laser powder bed fusion, (2) proposed strategies for mitigating residual stresses both before, during, and after fabrication, and (3) residual stress measurement by XRD. This will be followed by (4) a review of the aerospace applications of Ti6Al4V as well as previous work studying the anisotropic thermal expansion of this alloy and its thermomechanical and microstructural response when subjected to thermal cycling.

2.1. Metallurgy of Ti6Al4V

As with many titanium alloys, Ti6Al4V is a lightweight high strength structural material [1]. Moreover, Ti6Al4V is biocompatible hence its widespread use as a material for prosthetics and has excellent corrosion resistance [20].

As the name suggests, alpha-beta titanium alloys such as Ti6Al4V have a microstructure containing both the hcp α-phase, typically stable at room temperature in pure titanium, as well as the bcc β-phase, which appears at roughly 888°C in pure titanium [1]. Ti6Al4V contains aluminum

as an α-stabilizer and vanadium as β-stabilizer in order to reach a stable alpha-beta microstructure for a wide temperature range [1]. One advantage of Ti6Al4V which makes it especially attractive for laser based additive manufacturing processes compared with other titanium alloys is its relatively reasonable weldability [1].

There are several technical and metallurgical guides available on Ti6Al4V and on titanium and titanium alloys in general, and the reader is referred to these for additional detail concerning the properties of this alloy.

2.2. LPBF Process

The process of additive manufacturing can be subdivided into many different techniques based on variations in the fundamentals and/or the precise workings of the process. The scope of this review is limited to laser manufacturing processes, the most popular of which are selective laser sintering (SLS) and laser powder bed fusion (LPBF). Both of the aforementioned techniques employ high power lasers capable of achieving extremely high temperatures, thus making them ideal for the additive manufacturing of metal systems. SLS and LPBF are both powder bed techniques, differing slightly in their specific applications but retaining the same basic operating principle [9].

Figure 2-1 shows a schematic of the LPBF process. The same schematic can be applied to SLS as well. A single layer (with predefined thickness) of the desired powder is deposited in the process area on a solid plate of similar composition termed the base plate or substrate. The base plate itself sits atop a piston which moves in the vertical *z*-direction [9]. In order to determine the appropriate thickness for the initial layer as well as the subsequent layers, the laser parameters affecting the penetrating depth must be well understood. A number of these parameters will be discussed in a

further section of the report. The laser is guided using an optical fibre, and scans along the horizontal *x*- and *y*-directions in which the laser head is free to move [9].

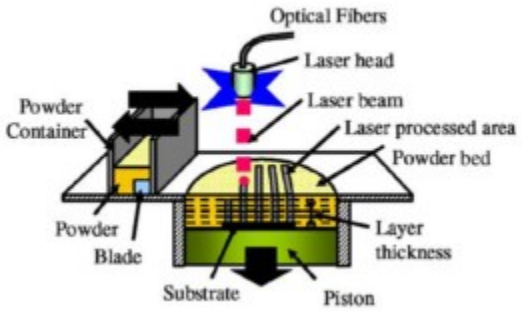

Figure 2-1: Schematic drawing of the LPBF process (image taken from [9])

In the case of LPBF, the laser can be either pulsed or continuous. The advantages of each are still under study. The basis behind each case, however, remains identical: the laser melts the powder, which then solidifies as the laser continues along its raster path to the next area of unmelted powder on the current layer [9]. Thus, a theoretically fully dense layer is formed. This method differs from SLS in that the laser employed is not powerful enough to fully melt the powder, instead effectively sintering the particles together [9]. Again, in both LPBF and SLS, once the first layer is completed (fully densified), the piston controlling the depth of the powder bed descends according to a set layer thickness (which can be tailored based on desired properties). A *sweeper* or *roller* adds extra powder to the piston atop the previous layer, and ensures a flat surface. The process repeats these steps in a layer-by-layer fashion until the final shape is obtained. At this point in the process, the completed component is ejected from the machine and removed from the base plate using the desired machining process (typically wire EDM or a standard band saw) [9]. A CAD drawing supplies the specifications of the component to the LPBF or SLS machine.

While additive manufacturing, by its design, is used in order to drastically reduce costs associated with post-processing machining and thus wasted material, a number of post-processing options are often nonetheless employed to ensure that the final component meets the stringent specifications set by its intended use. Due to the nature of powder-based processes, the outer surfaces will have a certain degree of surface roughness following SLS or LPBF. Thus, a light machining step is commonly included for surfaces that will be in contact with other surfaces or components during use. Additionally, in order to reduce porosity and/or residual stresses, a post-processing heat treatment is recommended [13]. The details and drawbacks of the latter are explained more in-depth in Section 2.5.3.

2.3. Residual Stress Measurement by XRD

X-Ray diffraction (XRD) is a relatively easy and inexpensive technique commonly used for measuring residual stresses. XRD is classified as a non-destructive technique, though is not as readily available as many destructive techniques such as hole drilling due to the still higher cost and size of the equipment. Moreover, since it is a diffraction technique, the sample must be crystalline [21]. XRD is an extremely popular technique and as such several in-depth guides have been written explaining the use of this technique for residual stress measurements. Below is a brief summary of the main points to consider.

XRD can be used to measure both macro and micro residual stresses, but can generally only achieve very shallow depths, especially in more dense materials such as Ti and Ti alloys, and is thus more suitable for surface and near surface residual stress measurements. Depth profiling can however be achieved if layers are removed after each measurement, though this technique then becomes a destructive measurement technique [21].

The principle behind the technique involves measuring elastic deformations in the crystal lattice using Bragg's law. A crystal containing residual stresses will have lattice spacings which differ from a nominally unstrained material of the same composition. On the XRD pattern, this would correspond to a shift in peak positions. Thus, especially for a full triaxial stress analysis, it is important that absolute unstrained peak positions are known prior to the analysis [22]. Strain measurements are made directly from precise measurements of the peak shift compared with the unstrained sample with the help of certain mathematical relationships [22]. Generally, the strain ϵ_ψ at any angle ψ can be calculated using the relationship

$$\epsilon_\psi = \frac{d_{\phi\psi} - d_0}{d_0}$$

where d_0 is the unstrained lattice spacing, and $d_{\varphi\psi}$ is the lattice spacing at the plane at angle $\varphi\psi$ to the surface. Using Hooke's law and Poisson's ratio, the calculated strain can be converted to stress values [22].

There are several experimental methods that can be employed to measure residual stress in XRD, the most popular of which being the $Sin^2\psi$ method. With this method, multiple angles of ψ are used, and values of $Sin^2\psi$ are plotted against the lattice spacing 2θ [21, 22]. By using the gradient of the plotted curve in conjunction with the material's elastic properties, the residual stress σ_ϕ can be calculated. The equation is given by:

$$\sigma_\phi = \left(\frac{E}{1+\nu}\right) m$$

where m is the gradient of the previously mentioned curve [22].

2.4. Effects of Residual Stresses on Properties

Residual stresses, especially tensile residual stresses, are known to negatively impact a number of properties of a material, hence the importance of reducing as much as possible the magnitude of these stresses. First and foremost, high values of residual stresses can elevate the probably of crack and microcrack formation and crack propagation within a solid component during fabrication or during use of the component [10, 17, 19, 23-25]. Quench cracking and stress-corrosion cracking have been identified as failure modes attributable primarily to high values of tensile residual stresses [21].

Residual stresses are also known to have an impact on the fatigue life and fatigue crack initiation/growth of a component [13, 19, 21, 26]. In a recent study by S. Leuders et al., the contribution to reduced fatigue life by high values of residual stresses was measured [13]. It was found that while porosity was the main factor by a large margin, residual stresses developed during LPBF contributed to a tenfold decrease in high cycle fatigue life in Ti6Al4V when compared with an identical stress-relieved sample [13].

Finally, high values of residual stresses approaching and exceeding the yield strength of a given material have been shown to cause deformations [10, 19, 23]. These deformations can cause several issues during fabrication, such as premature separation of the component from the base plate [17], and during the lifetime of the component. Depending on the dimensional tolerances set by the component specifications, even very small deformations can render a component completely useless.

2.5. Residual Stresses in LPBF

Due to the nature of the process, residual stresses in LPBF and SLS originate entirely from thermal sources. In a study by P. Mercelis and J.P. Kruth these sources are explored and their mechanisms explained [10]. The two principle mechanisms involved are (1) the temperature gradient mechanism (or TGM) [10, 21], and (2) the effects of the cooling phase on the molten layer [10]. The latter applies only to LPBF, as there is no bulk molten phase in the sintering-based process.

The effects of the TGM revolve around the high temperature area at and around the laser spot. A potentially very steep temperature gradient develops at this area due to the extremely high heat input and thus rapid temperature increase directly on the laser spot at the surface of the powder bed and the comparatively slow heat conduction to the surrounding area. In this initial state, the top layer would expand except for the underlying material which prevents the expansion. This effect results in compressive elastic strain, and plastic compressive deformation once these strains reach the yield strength of the material [10]. In the case of a simple metal sheet, this would be seen as a deformation away from the laser beam as shown in Figure 2-2. Similarly, during the cooling phase this same mechanism causes a tendency for deformation towards the laser beam due to shrinkage of the upper layer. This mechanism does not involve a molten state, and thus can apply to both LPBF as well as SLS [10].

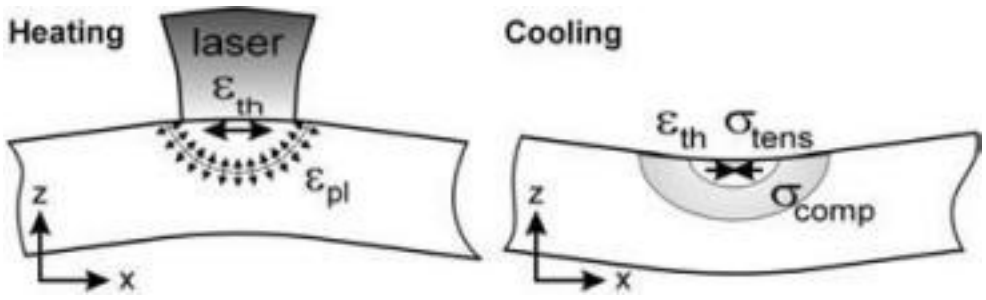

Figure 2-2: Drawing depicting the deformation mechanisms occurring by the TGM (image taken from [10])

In LPBF, the second mechanism is present due to the presence of a molten metal phase. As the molten phase solidifies, shrinkage occurs. Because the underlying solid layers become bonded with the upper layer at this point, this shrinkage is inhibited, thus causing tensile residual stresses to appear in the top layer while compressive stresses are introduced in the underlying layers [10].

The onset of residual stresses in LPBF is controlled by numerous different variables. These variables can be separated into two distinct categories based on their origins: process parameters, and design parameters. Process parameters will encompass all variables related to the LPBF equipment and to variables controlled during the process phase, while design parameters will focus on external variables which would be controlled during the planning and design phases of the individual components. This distinction is important to make as, with the exception of a few of the more ambiguous variables, the former can be applied globally while the latter occur on a case-by-case basis depending on the individual components.

2.5.1. Process parameters

As mentioned above, this subsection will deal with variables controlled during the process phase. This will include all laser parameters, parameters related to the base plate as well as to layer control, part orientation, and any atmospheric conditions within the LPBF enclosure, limited to those variables whose effects on residual stresses have been studied.

Laser parameters

For the most part, the effects of laser parameters on residual stresses are not extensively studied or are ignored. This appears to be largely due to the fact that many of these parameters such as laser power and hatch spacing which control energy density are controlled strictly to encourage proper and complete melting of the metal powder, to avoid balling effects, and to limit porosity as much

as possible [27]. Because these parameters affect energy density however, which directly influences temperature gradients, it can be surmised that they would at least have a minor effect on residual stresses.

The effects of some laser parameters on residual stresses have been studied, such as the laser scanning speed, and the scanning strategy, the latter much more than the former.

One set of experiments has shown that an increased laser scanning speed can cause a decrease in residual stresses [24]. The cause is not entirely explored by the authors but it is most likely due to energy density and temperature gradient effects.

For the case of scanning strategy, research has been fairly significant in recent years. Scanning strategy is defined as the path which the laser takes as it irradiates a given layer in the LPBF process. The simplest of these scanning strategies are the X-X (back and forth horizontally), Y-Y (back and forth vertically), and X-Y (alternation of X-X and Y-Y at each layer) patterns (Figure 2-3) [16].

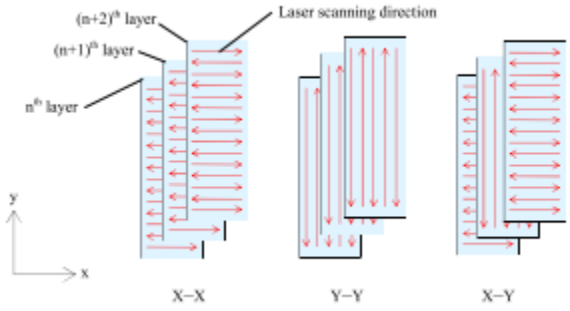

Figure 2-3: From left to right, X-X, Y-Y, and mixed X-Y scanning patterns (image taken from [16])

Much like other laser parameters, the scanning pattern affects temperature gradients and energy density. However, it is more the shape of the curves of these functions over time that is altered, as opposed to their magnitudes as with other parameters, as the scanning pattern simply alters the

frequency at which areas of the sample will receive direct or indirect heating from the laser. In most cases, it is important to consider the geometry of the sample in conjunction with the scanning pattern. In a recent study by M.S. Abdul Aziz et al. [16], tests were done on simple rectangular components built using these three simple scanning patterns. The sample built with the Y-Y pattern (which in this case corresponded with scanning along the longer edge of the rectangle) showed the highest recorded temperatures in the substrate with correspondingly high residual stresses. Both the samples built using the X-X and using the mixed X-Y pattern showed considerably lower temperatures and residual stresses, with the X-X (scanning along the short edge of the rectangle) sample showing the lowest of each. Consequently, the latter two patterns exhibited considerably less deformation due to these residual stresses upon separation from the substrate [16].

Furthermore, in another study performed by M.F. Zaeh and G. Branner [17], an *island scanning* strategy (Figure 2-4) is investigated and compared with the three simple patterns outlined previously, again on a simple rectangular shaped component. It is explained that this method would exhibit lower residual stresses due to an "alternating annealing of single islands", which does not occur in the more conventional linear scanning patterns [17].

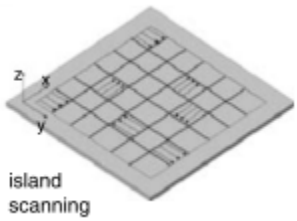

Figure 2-4: Island scanning strategy (image taken from [17])

In nearly all cases tested, it was shown that samples built using this island scanning strategy had lower residual stresses, while samples built using a linear scanning pattern along the long edge of the rectangular component showed the highest values of residual stresses [17].

Base plate control

The base plate, defined as the substrate upon which the component is built, is a necessary starting point in the process in order to avoid the first layer of powder being joined with the piston. As such, for much of the process, the base plate must be considered as part of the larger build and thus can influence various properties during processing such as residual stresses.

There are a number of ways in which properties of the base plate can affect the build-up of residual stresses in LPBF. Most importantly are its dimensions, as well as the choice of material. For both cases, what is observed is less of a direct effect on the residual stresses themselves than it is an effect on residual stress-induced deformations in the part. This can be explained by the fact that the base plate acts as a stiffening element for the component [10]. The effect of base plate thickness on residual stress-induced deformations has be examined in a study by P. Mercelis and J.-P. Kruth, and it was found that an increased thickness leads to lower residual stresses in the base plate and a more uniform distribution in the component, and thus less distortion upon separation in both the base plate and the component [10]. A number of separate studies confirmed the relationship of base plate height and distortions in the component, one adding that the magnitude of residual stresses in the top surface of the part varied very little with varying base plate height (Figure 2-5) [16, 28].

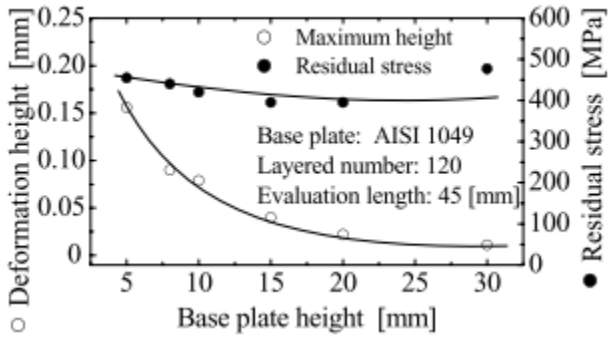

Figure 2-5: Effect of base plate height on component deformation and residual stresses at the top layer (image taken from [28])

In the case of the base plate material choice, deformations in the component are increased or decreased depending on the mismatch of linear coefficients of expansion between the component and the substrate while residual stress values can be controlled by the base plate's thermal conductivity [16]. In a study by M.S. Abdul Aziz et al., it is explained that thermally induced stress values in the component can be reduced by using a substrate with a lower thermal conductivity [16]. The lower thermal conductivity would cause more heat to remain in the component, thus increasing the maximum temperatures observed. However, this also causes temperatures throughout the component to be more consistent, and therefore lowering the thermal gradient [16]. It is crucial to understand that the choice of material cannot differ too greatly from the material used for the component itself. A too large mismatch in coefficients of thermal expansion could cause cracking and thus separation of the component from the base plate, while an incompatible material may cause corrosion at the interface.

Layer control

Layer thickness as well as the number of layers play a significant role in the build-up of residual stresses in LPBF according to recent research. In the case of layer thickness, the distance over which the heat input travels before reaching the previously melted layer is altered. A too great layer thickness would cause incomplete melting and porosity, and in extreme cases even complete

layer separation, all of which can have disastrous effects on various mechanical properties [9, 11]. In the same manner, the layer thickness directly affects the shape and magnitude of the thermal gradient. In a study by M.F. Zaeh and G. Branner, the effect of layer thickness on component deformation is explored, and it was determined that a greater layer thickness (within acceptable values so as to avoid the issues outlined above) leads to less deformations in the part (Figure 2-6) [17]. This is due to the fact that much higher temperatures were observed within thinner layers because of the reduced volume over which the heat can be conducted [17]. Unfortunately, residual stress values were not directly measured in this study.

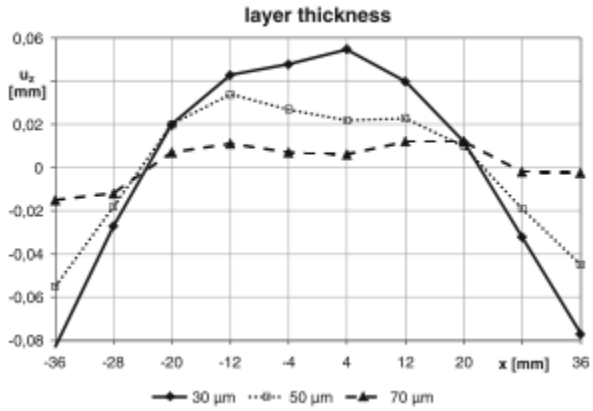

Figure 2-6: Effect of layer thickness on component deformation (image taken from [17])

In terms of the number of layers, this is directly influenced by a function of both the layer thickness and the height of the component. This variable is more difficult to classify as either a process or a design variable seeing how it is influenced by both sources. In a study by T. Furumoto et al., it was found that a higher number of layers led to increased values of residual stress and increased deformation in the component, reaching a plateau after approximately 400 layers with a constant layer thickness of 50µm (Figure 2-7) [28]. A similar relationship had been seen by P. Mercelis and J.-P. Kruth, though the test was not conducted with as high values and so they did not report reaching a plateau [10]. In the latter case, it is explained that compressive stresses continuously

accumulated at the bottom layers of the component, which would be subject to relaxation upon separation from the base plate (Figure 2-8) [10].

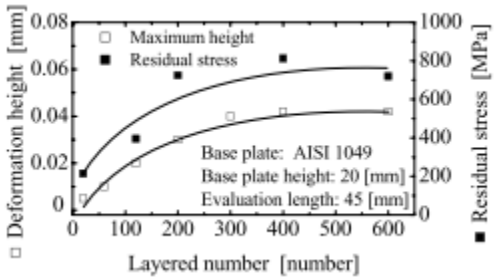

Figure 2-7: Residual stress and deformation magnitudes as a function of the number of layers for a chromium molybdenum steel powder (image taken from [28])

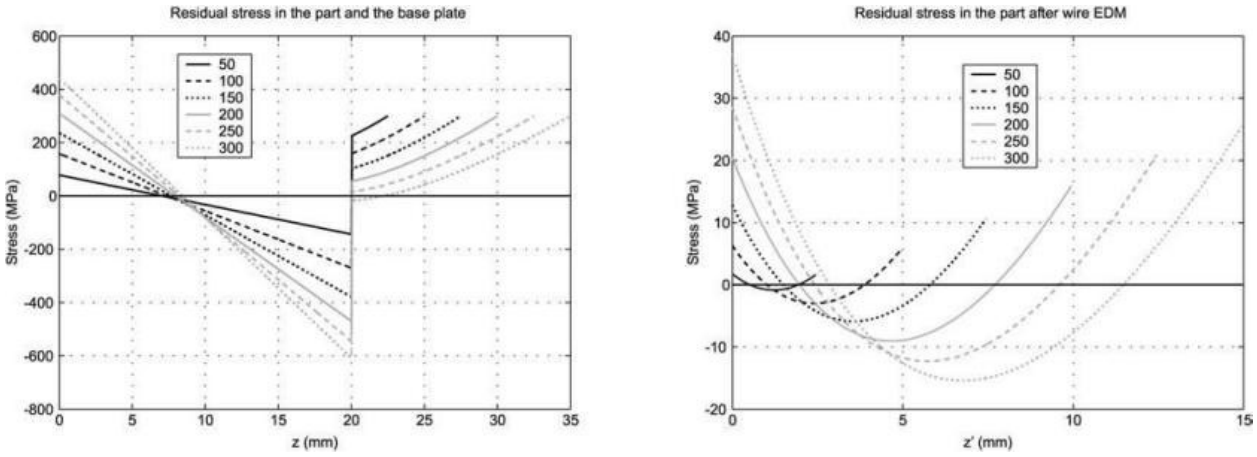

Figure 2-8: Effect of the number of layers on the residual stress profile (image taken from [10])

Process temperature

By preheating either the base plate, the build platform or potentially the entire LPBF chamber, the temperature gradients within the component can be drastically lowered. Currently, not all commercially available LPBF machines are equipped with the means to incorporate preheating. Nonetheless, for those equipped, preheating can be considered a process variable.

In both cases, the ideal preheating temperature would be as close as possible to the melting point of the chosen material within the LPBF chamber [13]. Maintaining these furnace-like temperatures, however, can be highly impractical as well as extremely costly, especially in the

case of high melting point materials such as Ti6Al4V. Care must also be taken in order to avoid any negative microstructural changes while operating at elevated temperatures.

Preheating solely the base plate or the build platform is more cost-effective than preheating the entire chamber, and has, as such, received much more attention. Preheating of the base plate has been shown to greatly reduce residual stresses at the boundary between the component and the base plate [28]. However, a separate study has demonstrated higher overall tensile residual stresses for a more complex geometry using an elevated base-plate temperature, which appears to go against the generally accepted theory [24]. These tests were performed in very different conditions, and as such are difficult to compare. Moreover, yet another study has demonstrated reduced plasticity of the component at an elevated initial platform temperature and therefore reduced deformations [17]. It should be noted however that in all cases, research has only been performed on small samples, and so the effectiveness of preheating the base plate or build platform on larger components with many layers, the topmost of which being not likely to benefit as much from the preheating, is unknown.

2.5.2. Design Parameters

As mentioned previously, design parameters are classified as whichever variables can be altered during the design phase. Thus, all variables discussed here are directly related to geometry and complexity of a given component. As such, their effects on residual stresses are more difficult to quantify as design choices are only limited by the intended functionality of the component and are made on a case-by-case basis.

Component height

The height of the component to be built directly influences the number of layers needed, the effects of which were discussed in Section 2.5.1. In many cases, the height of a component cannot be altered, as specifications may demand certain dimensions. However, if a component's dimensions are greater in one direction than another, a build orientation favoring a smaller number of layers can be considered.

Build orientation

The build orientation is defined as the angle at which a component is built with regards to its geometry. Thus, the build orientation essentially affects the area of each layer as well as their angle respective to the geometry. A rectangular shaped component built with its long edge laying against the base plate would be considered as having a horizontal *x*-direction build, while the same component built with its short edge resting on the base plate would have a vertical *z*-direction build. Build directions at any angle are technically possible, limited to the component geometry. Build direction is known to affect several important mechanical properties and is a root cause for anisotropy of properties in a given component [11, 29, 30].

As with the number of layers, the build orientation is difficult to classify as either a process or design variable. For simple geometries, the issue can be controlled during the process phase by determining in which orientation, be it vertically, horizontally, or at an angle, the component is to be fabricated. For more complex geometries, altering the build orientation simply changes which sections of the component will be built in which orientations. For example, a rectangular L-shaped cantilever may have its base built in the *x*-direction while its shaft is built in the *z*-direction (related to their respective long edges). The opposite may also be true of the cantilever is turned 90 degrees.

Thus, for complex geometries, it is important to consider the effects of build orientation during the design phase.

For the purpose of this report, build orientation will be considered a design variable due to its ambiguous and indirect effect on residual stresses. In fact, research into the effects of build orientation on residual stresses has been virtually non-existent thus far, which would lead one to believe that there is likely no direct relationship between the two. It has been shown however in a study by P. Mercelis and J.-P. Kruth that the residual stress profile in a component tends to be parabolic along the *z*-direction (in absolute coordinates) [10]. Thus it can be surmised that for complex geometries, altering the build direction would likely affect the locations of high tensile and compressive residual stresses within the component. Design considerations should be made in order to avoid large stresses being concentrated in less stiff thin-walled portions of a component if any are present.

Support structures

For complex geometries, it is sometimes necessary to incorporate support structures in the design in order to maintain structural integrity during fabrication and also to enable the construction of elevated sections which ordinarily lack a starting point in contact with the base plate, such as with large overhangs as demonstrated in Figure 2-9 [24]. Support structures require additional material and so come at a cost, but are necessary in cases such as these for a properly functioning part. Moreover, support structures act as a stiffening element for the affected regions of the component [24].

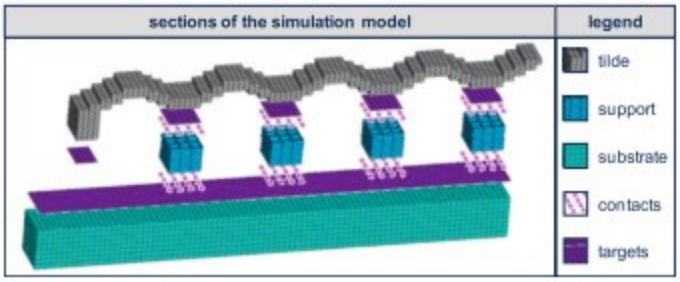

Figure 2-9: Example of a component which would require the use of support structures during fabrication (image taken from [24])

In a series of studies by T.A. Krol et al., the optimization of support structures is discussed in detail [24, 31, 32]. A semi-hollow approach is put forth which not only reduces the amount of material needed compared with a fully solid support, but can also be fine-tuned using predictive finite-element analysis (FEA) modelling to provide additional stiffening to more *at-risk* areas prone to high residual stresses [24, 32]. Thus, the design of the support structures is an important variable for reducing residual stresses in geometries which would require them. An example of how this can be accomplished is shown in Figure 2-10. Because the support structures will be removed from the final piece, residual stresses found within the support are of lesser concern, excepting if these would cause deformations to occur.

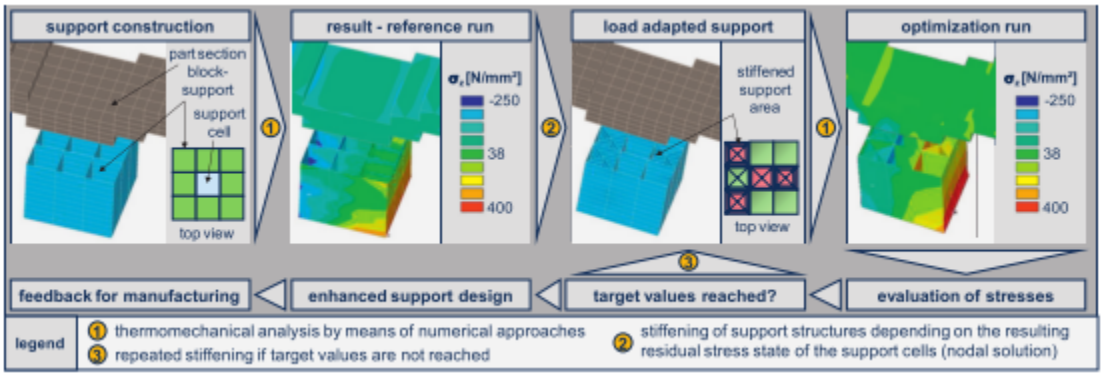

Figure 2-10: Example of how the support structures can be optimized in order to mitigate residual stresses (image taken from [24])

2.5.3. Mitigating residual stresses

Certain methods have been proposed for reducing residual stresses, such as the fine tuning of the numerous variables outlined in the previous section. All of these require good knowledge of how they influence the build-up of residual stresses, either by predictive modelling techniques or by experiment. Heat treatments, on the other hand, can be employed as a correctional method of reducing residual stresses, and in some cases have been shown to completely eliminate them [13].

Common heat treatments include stress-relief, annealing, and hot isostatic pressing (HIP), all of which are typically tailored to the thermal properties of the material in question. Stress-relief is a short, relatively low-temperature soak, with very little effect on the material's microstructure, making it ideal for reducing residual stresses, hence the name of the process. For Ti6Al4V, the stress-relief temperature is not strictly set, so long as it is sufficiently below the beta-transus temperature, which appears at approximately 950-1000ºC [1].

Annealing can have a wide range of temperatures, but is generally higher than the stress-relief regime and/or performed for longer. Compared with stress-relief, annealing is known to have a more noticeable effect on microstructure, and has also been shown to somewhat reduce porosity. In the case of Ti6Al4V, coarsening of the α-phase as well as the appearance of more substantial β regions can be seen [13].

Finally, HIP is a combination heat treatment with applied pressure. The result is a nearly complete removal of porosity, with substantial changes to microstructure. What is observed is further coarsening of the α-phase compared with annealing and more important growth of β regions [13].

In all cases, the heat treatment selected is highly dependent on the desired properties of the material. In LPBF and additive manufacturing processes in general, it is important to consider

however that heat treatments represent an extra processing step and thus an extra cost. Additive manufacturing is an attractive process due to the ability to fabricate components in as little as a single processing stage. In aerospace, this is represented by a drastically lowered buy-to-fly ratio. Thus, any additional processing step reduces the advantage of additive manufacturing over more conventional techniques. Moreover, heat treatments for large components are significantly more costly, and not always possible; therefore this does not represent a universal solution to the residual stress issue.

2.6.Thermal cycling and dilatometry

Depending on its particular application, a component may be subjected to a large number of heating and cooling cycles over the course of its lifetime. These cycles can vary in the rates of heating and cooling, the maximum and minimum temperatures observed, as well as the holding time at any maxima or minima. Material considerations are thus taken into account for the given component to account for its expected thermal regime. For example, if a component is expected to operate within a particular temperature range, a material will be chosen that suffers no irreversible changes to its microstructure or mechanical properties within that range. The component must also not fail for the given temperature gradients of the application (e.g. the appearance cracks or fracturing of the component). In many cases, regular maintenance will be performed at which point the early onset of a part failure or weakness can be detected.

Aside from the above, the thermal expansion or contraction of the components must be taken into account, and a proper tolerance allowed. For many applications, the tolerance is extremely important and must be great enough to prevent damage to the component itself and to the surrounding material, but also small enough such that the component can still perform properly [33].

In order to understand how a material will perform for a given set of thermal conditions, thermal cycling simulations are conducted. Dilatometers represent excellent tools for observing the behavior of a material for a given thermal regime. Coefficients of thermal expansion (CTE) are directly measured and allow for the prediction of tolerances, while material transformations can be detected by sudden and irregular changes to the CTE during dilatation [34-36].

2.6.4. Temperature limits for aerospace applications of Ti6Al4V

In aerospace, Ti6Al4V is considered mainly for lower temperature applications within the modern gas turbine engine, such as the low-pressure compressor region, as well as for some structural elements in the cockpit and landing gear [3]. However, variations in operating temperature are only expected to be significant in the former. In the low-pressure compressor region, temperatures are known to vary between room temperature at rest to between 300 – 450ºC due to creep considerations [37, 38].

In a study by M.J.R. Barboza et al., the creep behavior of Ti6Al4V between 500 – 600ºC under a constant load was investigated [39]. The samples tested had α-β Widmanstätten microstructure and average β grain size of 395 µm and α lath width between 3.2 – 4.0 µm. Both long- and short-range dislocation is observed, with a notably shorter long-range dislocation period at higher temperatures and stress, though the majority of the creep life appeared to be governed by a constant creep rate [39]. Creep curves obtained in this study are presented in Figure 2-11.

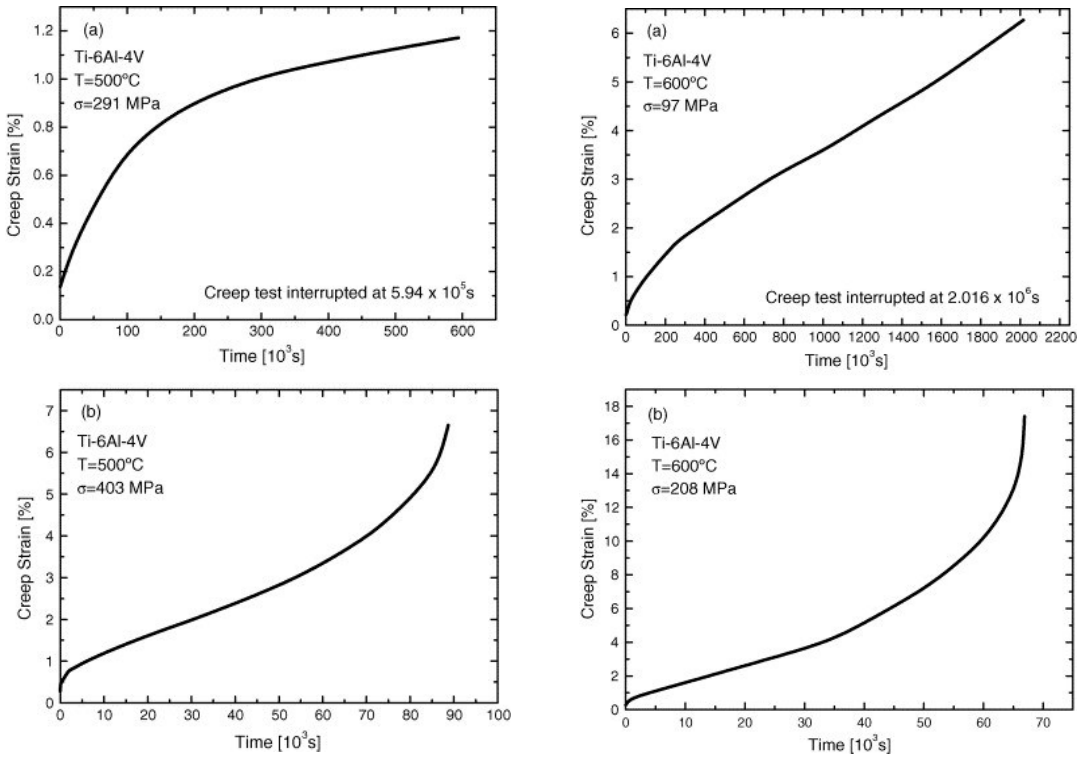

Figure 2-11: Creep curves obtained for Ti6Al4V tested at 500°C (left) and at 600°C (right) under various loading conditions [39].

The stress exponents n in the following relationship between the steady-state creep rate and temperature and stress

$$\dot{\varepsilon_s} = A\sigma^n \exp\left(-\frac{Q_s}{RT}\right)$$

where R is the gas constant, T is temperature, Q_s is the activation energy, A is a constant, and $\dot{\varepsilon_s}$ is the creep rate, were calculated at 11.3 at 500°C and 5.2 at 600°C. Furthermore, the threshold stresses were measured at 217.81 MPa at 500°C and 34.47 MPa at 600°C [39]. Similar results were reported in a study by L. Badea et al. in a series of creep experiments performed for temperatures ranging from 450°C to 600°C [40].

2.6.5. Thermal expansion anisotropy

In Ti6Al4V, thermal expansion does not occur uniformly for all crystal directions. Ti6Al4V has an HCP α-phase and a BCC β-phase, and the lattice parameters *a* and *c* of the α-phase are not equal. A representative schematic of the HCP unit cell is shown in Figure 2-12. The lattice parameter along the basal direction of the crystal (*a*) is smaller than the lattice parameter along the prismatic direction (*c*), and this is reflected in the thermal expansion for each of these directions. A number of studies have been published that discuss this expansion anisotropy, some specifically for Ti6Al4V as it has been shown to have anomalous expansion behaviour at low temperatures [41, 42].

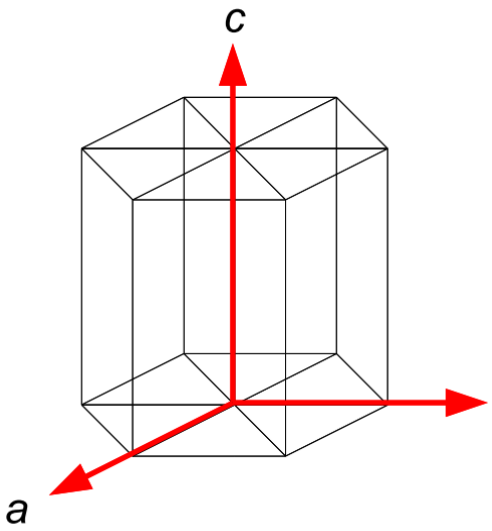

Figure 2-12: Schematic of the HCP unit cell with labelled lattice parameters (figure adapted from [43])

An early study conducted in 1968 by R.R. Pawar and V.T. Deshpande acknowledged the existence of an anisotropic expansion in Ti6Al4V [44]. The authors discussed previously reported findings and supplemented with their own results obtained through lattice expansion measurements by XRD. The temperature range observed, however, was limited from room temperature to 155°C. They reported coefficients of thermal expansion of approximately $9.5^{o}C^{-1}$ along the basal direction *a* and $5.6^{o}C^{-1}$ along the prismatic direction *c* [44].

This anisotropy is confirmed in a number of separate independent studies offering various explanations for the phenomena observed. V. Nizhankovskii et al. propose the proximity to an electronic topological transition as a possible cause for the anisotropic behavior at low temperatures and negative thermal expansion coefficient in the prismatic direction *c* observed at these temperatures as well [41]. P. Souvatzis et al. also report this negative CTE below 170K in the prismatic direction *c* and expanded on the work by V. Nizhankovskii et al., proposing that the anisotropy is due to the presence of a saddle point Van Hove singularity at the Fermi level [42]. A compilation of data points presented in the literature for the CTE of α-phase titanium is presented in Figure 2-13 . From this figure, it can be seen that thermal expansion in the basal plane *a* leads over expansion in the prismatic plane *c* at lower temperatures, while the opposite becomes true as higher temperatures are reached. The point at which this inversion occurs is speculative, but can be approximated based on the limited published data to lie in the range of 400-600K. [41, 42, 44, 45].

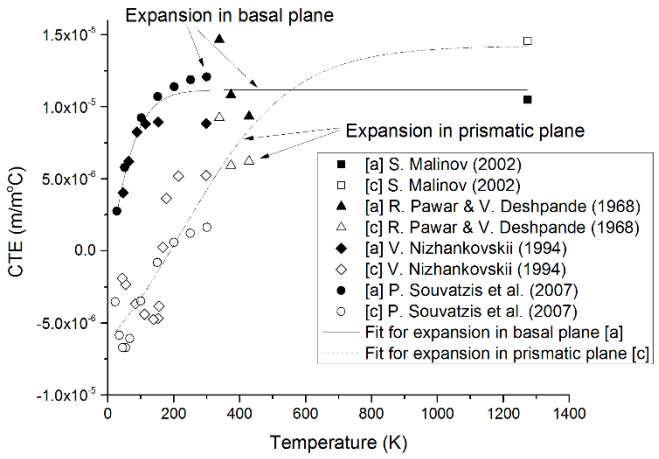

Figure 2-13: Literature values reported for the coefficient of thermal expansion of Ti6Al4V in the basal plane and the prismatic plane respectively, with an approximate fit showing a possible inversion point [41, 42, 44, 45].

2.6.6. Thermomechanical response of Ti6Al4V

Thermal cycling experiments are typically conducted in order to observe the thermomechanical or microstructural response of an alloy given a set of repeated heating and cooling cycles or in some cases one single heating/cooling cycle. The temperature limits and applied heating/cooling rates are usually determined by the specific application of the material and are intended to simulate a real life application.

To the authors' knowledge, there have been no thermal cycling studies performed on Ti6Al4V in the LPBF condition to date. However, a number of thermal cycling studies were performed for this alloy in the forged or wrought conditions [46-50]. In a study by S. Manikandan and S. Ramanathan, Ti6Al4V samples were heat treated and subjected to 500, 1000, or 1500 thermal cycles up to 450ºC for the purpose of measuring flow stress and hardness in hot compression tests at various temperatures [46]. It was found that the flow stress reaches a maximum after approximately 500 cycles and an increase of strength with increased of number of cycles was reported. Hardness was found to greatly increase up to 500 cycles after which point it continues to increase though at a much slower rate from 1000 to 1500 cycles [46].

Mechanical properties were measured following thermal cycling at greater temperatures in a study by M.N. Mungole et al., where cycling within specific phases of the alloy was performed [50]. Samples were subjected to thermal cycling from 100ºC to 950ºC for 50 and 100 cycles, from 100ºC to 875ºC for 50, 100, 150, and 200 cycles, and from 950ºC to 1150ºC for 50 cycles. It was found that thermal cycling in the two phase region caused a reduction in strength and ductility after 50 cycles with a subsequent increase after 100 cycles. Continuing to cycle up to 150 and 200 cycles caused a noticeable reduction in ductility. For experiments cycling from a two phase to single

phase (β) region (i.e. 950 – 1150ºC) did not appear to have an effect on strength, though ductility suffered greatly [50].

2.6.7. Microstructural response of Ti6Al4V

As mentioned previously, thermal cycling is also useful to determine the effect of repeated heating and cooling on the microstructure of a material, as this can greatly impact a given component's functioning and lifetime.

M.N. Mungole et al. studied the effects of repeated thermal cycling in two phase (100 – 875ºC and 100-950ºC) or single phase regions (950 – 1150ºC) on the microstructure of forged Ti6Al4V [50]. The initial microstructure is shown in Figure 2-14 and consists of an equiaxed grain structure with both α and β phases present [50].

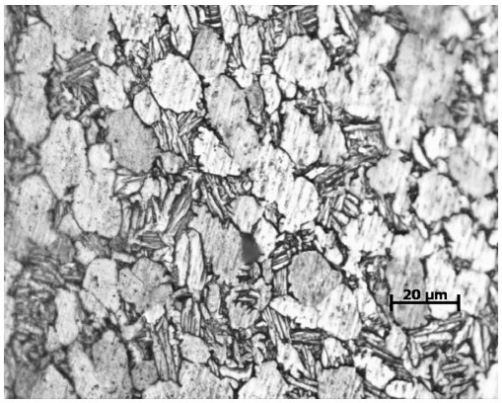

Figure 2-14: Initial microstructure of forged Ti6Al4V prior to thermal cycling (taken from [50]). Bright regions correspond with α phase while darker regions and feathery morphologies correspond with β phase.

Following thermal cycling from 100 – 950ºC, a drastic change in microstructure was observed, with the β volume fraction measured at 50% and 35% after 50 and 100 cycles respectively. The resulting basket weave structure with ensuing coarsening of the platelets after 100 cycles is shown in Figure 2-15 [50].

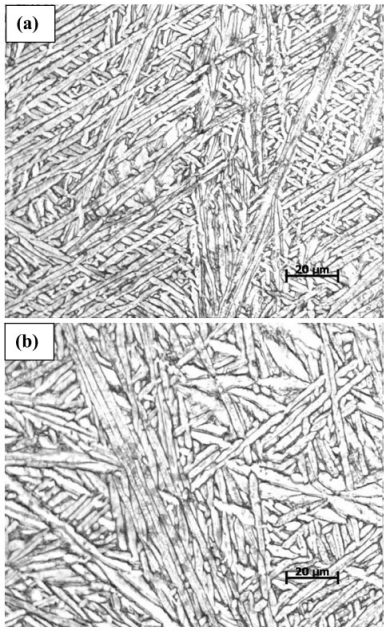

Figure 2-15: Microstructures of forged Ti6Al4V following thermal cycling from 100 – 950ºC after (a) 50 and (b) 100 cycles (taken from [50]). Visible coarsening of the platelets is observed after 100 cycles.

The microstructure following thermal cycling from 100 – 875ºC was similar to the above, though finer and more needle-like with a greater β phase fraction. Coarsening with an increased number of cycles was observed in this case as well [50]. Finally, when cycling from a two phase to a single phase (β) region (i.e. 950 – 1150ºC), a completely different microstructure from the previous thermal cycling regimes was obtained. Here, α and β phase were aligned unidirectionally when soaked for 3 minutes, and when soaked for 5 minutes α platelets aligned crosswise were observed with a much finer morphology than for the two phase thermal cycling. The microstructures are shown in Figure 2-16 [50].

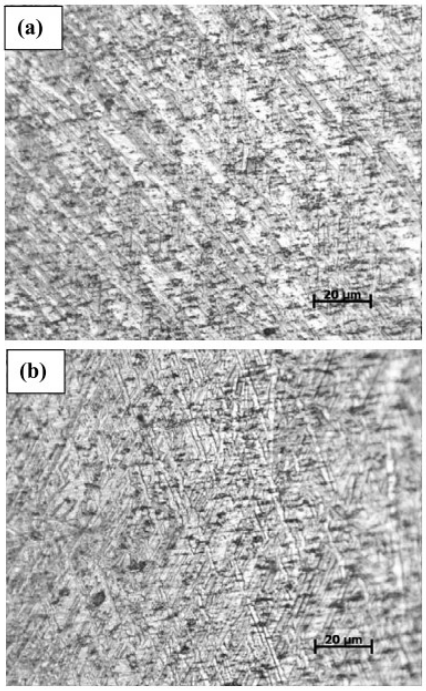

Figure 2-16: Microstructure of forged Ti6Al4V following thermal cycling from 950 – 1150°C for 50 cycles with a holding time at 1150°C of (a) 3 and (b) 5 minutes (taken from[50]).

In a separate study by P. Lv et al., changes in microstructure were observed for Ti6Al4V samples following low temperature thermal cycling in low-earth orbit (LEO) simulation conditions (-110 – 140°C) for 100, 200, 300, 400 , and 500 cycles [48]. The initial microstructure was a typical α-β lath structure (intergranular β). Significant elongation of the α platelets was observed after 300 cycles with the appearance of some cavities. After 500 cycles, the alpha grains became more rounded, a degradation in the β phase continuity was observed, and more cavities were reported with increased size. The microstructures are shown in Figure 2-17 [48].

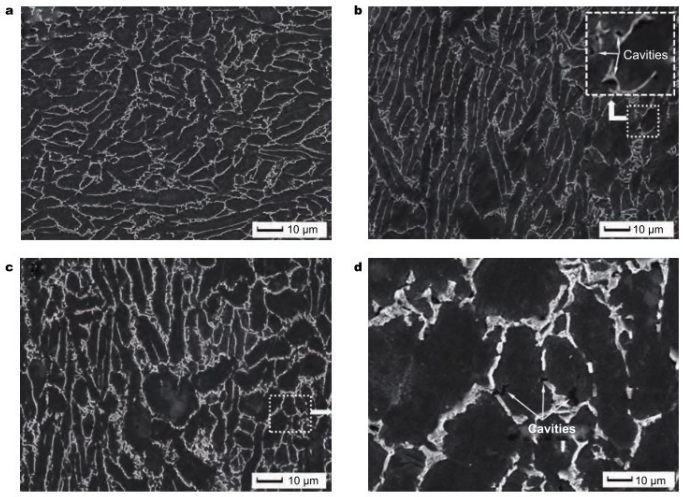

Figure 2-17: Microstructures of Ti6Al4V sample subjected to low temperature thermal cycling (-110 – 140°C): (a) before cycling, (b) after 300 cycles, and (c, d) after 500 cycles (taken from [48]).

Chapter 3 – Experimental Methodology

3.1. Introduction

This chapter provides a detailed overview of the various equipment used and procedures followed to obtain the results presented in Chapters 4 and 5. A brief summary of the manufacturing and post-processing procedures will be provided to better understand some of the process variables discussed in later sections. This will be followed by the analytical equipment and methods used to obtain the results presented in this thesis.

3.2. LPBF manufacturing

The device used to fabricate all samples studied in this project is known as a Concept Laser M2 Cusing unit. The device uses a 200 W Nd:YAG laser capable of fully melting a wide range of metallic powders including Ti6Al4V. Manufacturing is performed within a sealed chamber in an inert atmosphere and an integrated glove-box system to further reduce contamination when handling samples and raw powder. The M2 Cusing unit can fabricate samples on a build plate with dimensions up to 250 mm x 250 mm. Samples can be created up to 280 mm in height. The powder used was spherical Ti6Al4V ELI grade 23.

A series of Ti6Al4V rectangular tubes were fabricated in this manner, and are shown in Figure 3-1. These were designed with three variables in mind: (1) length of the tube, (2) thickness of the tube wall, and (3) angle of overhang. Lengths used were 25.4 mm, 50.8 mm, and 101.6 mm. Wall thicknesses used were 0.5 mm, 1.0 mm, and 2.0 mm. All samples in this subset were rotated along one axis such that an angle of overhang of 45^{o} is obtained. Thus, no additional support structures are required. An extra set of samples were printed with slightly varied dimensions to obtain angles of the walls at 53^{o} and 61^{o} to the horizontal respectively. A second set of reference samples were

printed for stress relief heat treatment for further comparison. All samples were analysed for residual stress induced deformations by the process described in Section 3.4.

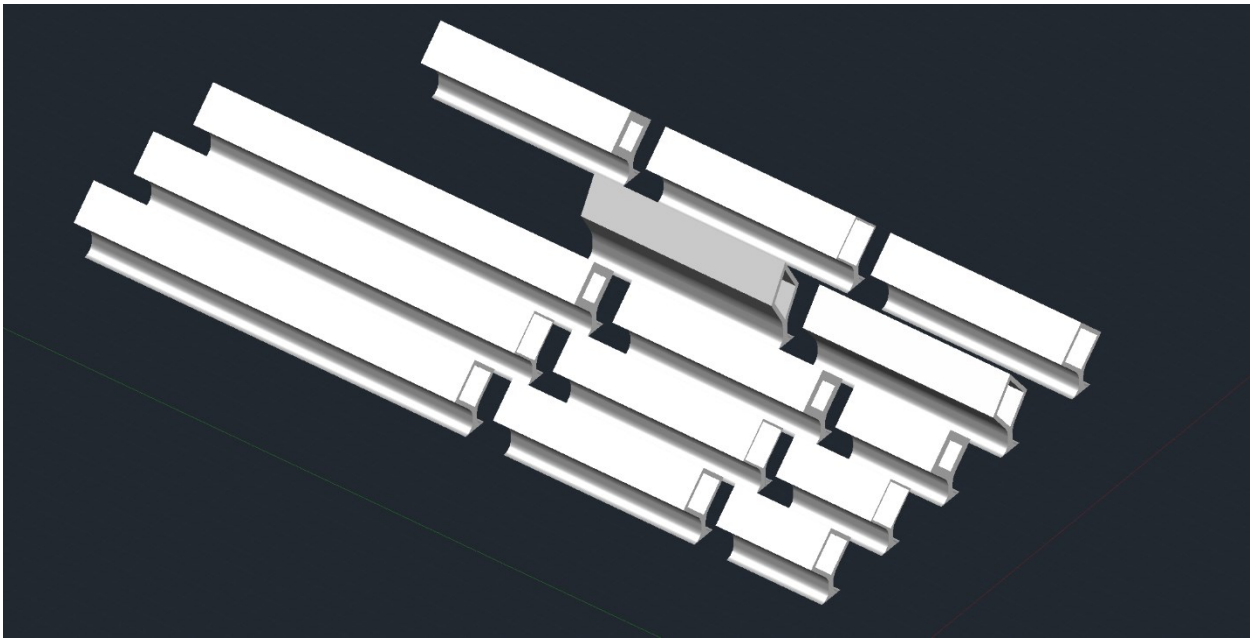

Figure 3-1: CAD drawing of the 14 rectangular tube samples under investigation.

For a separate study, dilatometer samples were extracted from previously fabricated Ti6Al4V specimens using the same M2 Cusing unit. The dilatometer samples were machined to a cylindrical shape with dimensions specified by the dilatometer manufacturer (3 mm diameter by 10 mm height). The original samples were fabricated in X, Z, and 45^{o} orientations respective to the base plate.

3.3. Post processing heat treatment

Three of the rectangular tubes described in Section 3.2 underwent a stress relief heat treatment following the AMS 2801 standard. The specimens from which the dilatometer samples were extracted underwent three possible heat treatments: (1) stress relief following AMS 2801, (2) mill annealing following AMS 2801, and (3) hot isostatic pressing (HIP) following ASTM F2924.

3.4. Deformation measurements

Deformations in the rectangular tube samples due to residual stresses were measured using an overhead Zeiss Spectrum II coordinate measuring machine (CMM) with a LDI SLP500 laser scanning head. Initial measurements were taken while samples were still attached to the base plate and as such were limited to the top surfaces of each sample. The data obtained was overlaid with the original CAD to obtain a net map of deformations. Measurements were again taken using the same instrument following removal of the samples from the base plate.

3.5. Residual stress measurements

Residual stresses were measured by XRD using a Cu-source Bruker D8 Discover X-ray diffractometer with k_α = 1.54 Å. Measurements were taken on the 110 and 112 α-Ti peaks (2θ= 59.90^o to 63.30^o and 75.00^o to 76.90^o respectively). A pseudo-Voigt profile lineshape function was used to then calculate the actual residual stress values. Residual stress measurements were taken on the certain rectangular tube specimens following removal from the base plate as well as on dilatometry samples following thermal cycling.

3.6. Dilatometry

Dilatometry and thermal cycling was performed using a Linseis L78 R.I.T.A. Quenching Dilatometer on the samples described in Section 3.2. Fused silica pushrods with near-zero coefficient of thermal expansion (CTE) were used to eliminate external factors, and the experiments were performed under a pre-purified helium (99.995%) shielding environment. Temperature profiles were selected with temperature limits of 25 – 750 ^{o}C and 25 – 400 ^{o}C. In each case, 50 cycles were performed with 27 and 16 ^{o}C/s heating and cooling rates respectively

controlled by an induction coil and high precision thermocouples, and with holding times of 5 minutes at the maximum and minimum temperatures.

3.7.Microstructural analysis

Samples prepared for microscopy (either SEM or optical) were prepared using the following grinding/polishing procedure:

Table 3-1: Grinding/polishing procedure.

	Grinding media	Time
1	Grinding paper (SiC – 240 grit)	3 min (by hand)
2	Grinding paper (SiC – 400 grit)	3 min (by hand)
3	Grinding paper (SiC – 600 grit)	3 min (by hand)
4	Grinding paper (SiC – 1200 grit)	3 min (by hand)
5	Vibromet (colloidal SiC)	240 min

Optical microscopy was performed on polished cross sections using a Clemex microscope. For microstructural analysis, surfaces were first etched using Kroll's Reagent (2% HF, 6% HNO_3 and 92% distilled water for 20 seconds). Higher magnification imaging was performed using a Hitachi SU3500 SEM. Crystallographic texture was obtained by EBSD using the same Hitachi SU3500 microscope and analysed using Oxford Instruments-HKL Channel 5 software.

Chapter 4 – Geometric Distortions in Ti6Al4V Fabricated by Laser Powder Bed Fusion

Preface

Geometric Distortions in Ti6Al4V Fabricated by Laser Powder Bed Fusion is a comprehensive study, the results, conclusions, and procedures of which are detailed in Chapter 4. This article is intended for publication in the year 2018 and presents the effects of various design parameters on the magnitudes of thermal stress induced deformations. Below is the expected citation for the article:

J. Danovitch, J. Choi, N. Chekir, J. Squire and M. Brochu. *Geometric Distortions in Ti6Al4V Fabricated by Laser Powder Bed Fusion*. *Article intended for publication.* 2018

Abstract

The current study is intended to provide a better understanding of the effects of various design variables on the magnitude of thermal and residual stress-induced distortions for Ti6Al4V components, an important industrial alloy. A series of angled rectangular hollow tubes were produced with varying wall thickness, length, and wall angles. Wall thickness was shown to non-linearly affect the magnitude of distortions occurring during fabrication. Sample length had a noticeable effect on deformations as well, though the trend appeared to become less important with increasing length. The angle of overhang was also studied, and a trend of increasing deformations with increasing angle (i.e. decreased degree of overhang) was observed, owing to the reduced width of the walls in each layer as well as overall trends in residual stress generation with the number of layers. Following separation from the base plate, further deformations in untreated samples were observed due to the relaxation of residual stresses. Surface residual stress

measurements showed greater residual stresses remaining in the sample with the greatest wall thickness, which supports the relaxation distortions observed.

KEYWORDS: Ti6Al4V, residual stress, additive manufacturing, powder bed fusion, distortions, stiffness

4.1. Introduction

Additive manufacturing (AM), commonly referred to as 3D printing, is a class of techniques that allow for the fabrication of inherently complex shapes in a layer-by-layer fashion. One such technique is laser powder bed fusion (LPBF), where a high power laser is used to selectively melt specific areas on a bed of metallic powder. This technique, along with other similar methods such as electron beam melting (EBM) and direct energy deposition (DED) have been shown to produce, under the appropriate parameters, full density components [9]. Due to the ability to create highly complex structures, AM has gained a great deal of attention in recent years as a potential fabrication method in the aerospace and biomedical domains [2, 51].

The numerous thermal gradients imposed during fabrication lead to one of the main obstructions to widespread adoption of these AM techniques; the high rates of heating and cooling applied generate residual stresses, known to accumulate to the extent of sometimes exceeding the yield strength of the material [8, 10, 16, 24]. When this occurs, the structure begins to deform, limiting the usefulness of the final product and in extreme cases causing complete build failure [17, 52]. These residual stresses can be mitigated by a number of means, as shown in previous studies, such as through the use of localized support structures which act as a stiffening element and allow for some of the local heat to be dissipated [24], preheating of the base plate so as to reduce the heating and cooling rates observed [13, 17, 24, 28], or applying a stress relief heat treatment following

fabrication [13]. Each comes with their own disadvantages however. Support structures are not always possible depending on the geometry of the part, and they represent added material which increases the time and cost of the build thereby reducing the benefits of using AM. Furthermore, parts built with support structures require an additional machining step following fabrication in order to remove them. Depending on the material, a certain maximum angle of overhang exists at which point the use of support structures becomes necessary to prevent build failure [53]. Previous studies have clearly demonstrated the effect of support structures on the reduction of residual stresses in LPBF [17, 24, 54]. Moreover, the removal of support structures after fabrication represents an additional processing step. Preheating of the base plate can be very costly to maintain due to the high temperatures required throughout the building process. Many materials, such as Ti6Al4V, are more susceptible to oxidation at higher temperatures as well. And finally, applying a stress relief heat treatment, while necessary to effectively remove the residual stresses from the components, does not prevent distortions from occurring during fabrication.

By understanding how certain shapes and materials behave under high thermal cycles, it becomes easier to predict their effectiveness and whether or not irreversible deformations will occur given a known set of conditions. The following study focuses on observing the effects of residual stresses on Ti6Al4V with various geometries that might be considered at-risk for residual stress-induced deformations in LPBF and provides guidelines for whether or not additional means would be required in order to make certain builds feasible, and therefore allow for more cost-effective decision-making. Ti6Al4V was chosen as the material for this study as it is a relatively well established alloy in AM, specifically LPBF, and is particularly susceptible to thermal strains due to its relatively low density and thermal diffusivity [55].

4.2. Experimental Procedure

A set of 14 hollow Ti6Al4V rectangular tubes were designed for printing by LPBF with the objective being to measure and obtain maps of deformations caused by thermal and residual stresses as a function of slight variations in part geometry. The three geometric features observed were wall thickness, sample length, and angle of overhang. Wall thicknesses of 0.5 mm, 1.0 mm, and 2.0 mm were tested. For each thickness, rectangular tubes with lengths of 25.4, 50.8, and 101.6 mm were considered. Each of these samples was built with an angle of overhang of 45^{o}. Two additional samples with angles of 53^{o} and 61^{o} were designed. For each length, regardless of wall thickness and angle of overhang, the outer dimensions of each wall are identical. Finally, a second set of 50.8 mm long reference samples built with an angle of overhang of 45^{o} for each of the studied wall thicknesses was set aside for eventual stress relief heat treatment with the objective of being able to compare with the as-built samples upon separation from the base plate for further deformations caused by the relaxation of residual stresses. A summary of the samples built is presented in Table 4-1, and the relevant dimensions are depicted in Figure 4-1. The CAD drawing containing the 14 samples described above is presented in Figure 4-2.

Table 4-1: Summary of samples studied.

Specimen #	Wall thickness (mm)	Sample length (mm)	Angle of overhang	Dimensions of outer walls (mm)	Heat treatment
1	0.5	25.4	45º	25.4 x 10	
2	0.5	50.8	45º	50.8 x 10	
3	0.5	101.6	45º	101.6 x 10	
4	1.0	25.4	45º	25.4 x 10	
5	1.0	50.8	45º	50.8 x 10	
6	1.0	101.6	45º	101.6 x 10	
7	2.0	25.4	45º	25.4 x 10	
8	2.0	50.8	45º	50.8 x 10	
9	2.0	101.6	45º	101.6 x 10	
10	1.0	50.8	53º	50.8 x 10	
11	1.0	50.8	61º	50.8 x 10	
12	0.5	50.8	45º	50.8 x 10	Stress relief
13	1.0	50.8	45º	50.8 x 10	Stress relief
14	2.0	50.8	45º	50.8 x 10	Stress relief

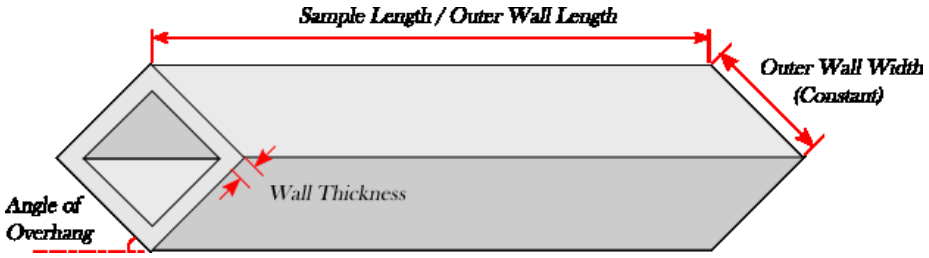

Figure 4-1: Sample schematic showing relevant dimensions.

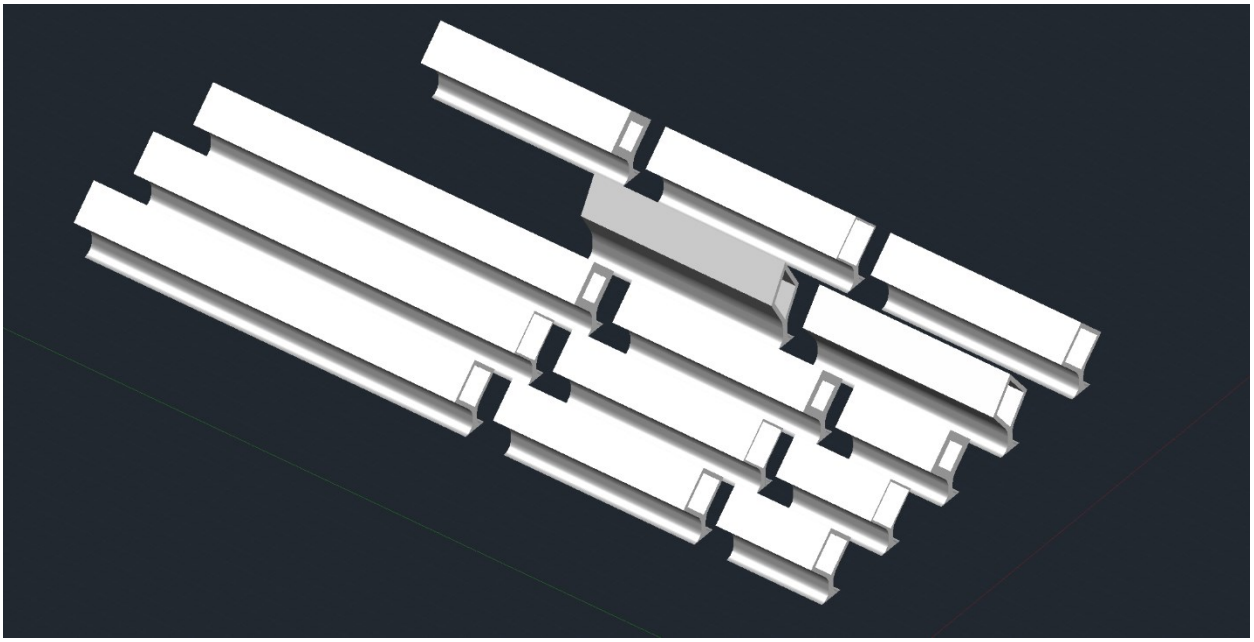

Figure 4-2: CAD drawing of the 14 rectangular tube samples under investigation.

This particular geometry was selected for its susceptibility to distortions during fabrication. The 45° angle tilt of the rectangular tubes was chosen as this would permit the samples to be fabricated without the use of support structures. Additionally, hollow thin-walled tubes such as those considered in the current study are especially susceptible to thermal stresses and residual stress build-up as heat conduction is drastically minimized. Thus, the geometries observed in this study can be considered particularly at-risk of deformations in LPBF.

All samples were fabricated on a single build plate at Edmit Inc. (Châteauguay, QC) by LPBF using a Concept Laser M2 Cusing unit with standard building parameters including island scanning strategy for Ti6Al4V and spherical Ti6Al4V ELI grade 23 powder as supplied by the machine manufacturer. Those samples which have undergone heat treatment were stress relieved following the AMS 2801 standards (593°C for 2 hours [56]).

Deformation measurements were performed using a Zeiss Spectrum II coordinate measuring machine (CMM) equipped with a LDI SLP500 laser scanning head. Initial measurements were

performed on the top surfaces of the deformed rectangular tubes while still attached to the base plate. This was done in order to observe the detrimental effects of thermal and residual stresses arising during the LPBF process. The data obtained was then overlaid with the original CAD design and a net deformation map could be created. Following this, the samples were separated from the base plate and a new set of deformation measurements was obtained specific to the relaxation of built-up residual stresses.

A Cu-source Bruker D8 Discover X-ray diffractometer ($k_\alpha = 1.54$ Å) was used to measure residual stresses on select areas of a number of rectangular tube samples. This was performed following separation from the base plate on both stress relieved and as-built samples. Diffraction patterns were collected for the 110 peak from $2\theta = 59.90^o$ to 63.30^o. A pseudo-Voigt profile lineshape function was used to calculate residual stress values from the diffraction pattern.

4.3. Results and Discussion

4.3.1. Geometric distortions as a function of wall thickness and sample length

A total of 14 Ti6Al4V samples were fabricated by LPBF. Figure 4-3 and Figure 4-4 show photographs of the printed samples attached to the base plate. Following fabrication and prior to separation from the base plate, deformations can easily be identified to the naked eye on all 0.5mm and 1.0mm wall thickness specimens.

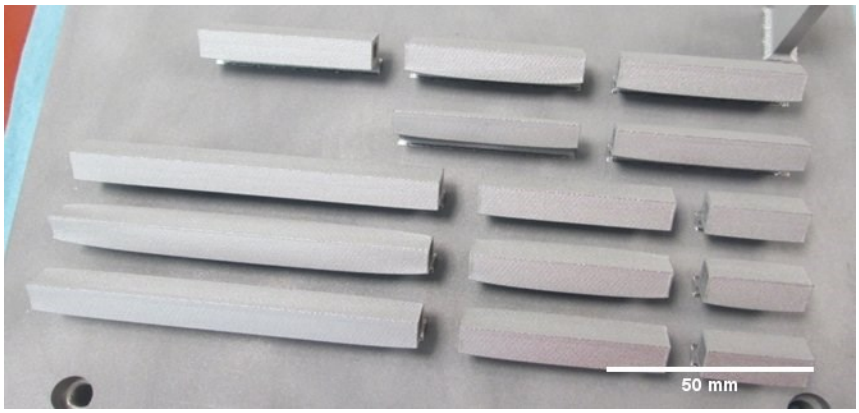

Figure 4-3: Top down view of rectangular tube samples as printed attached to the base plate.

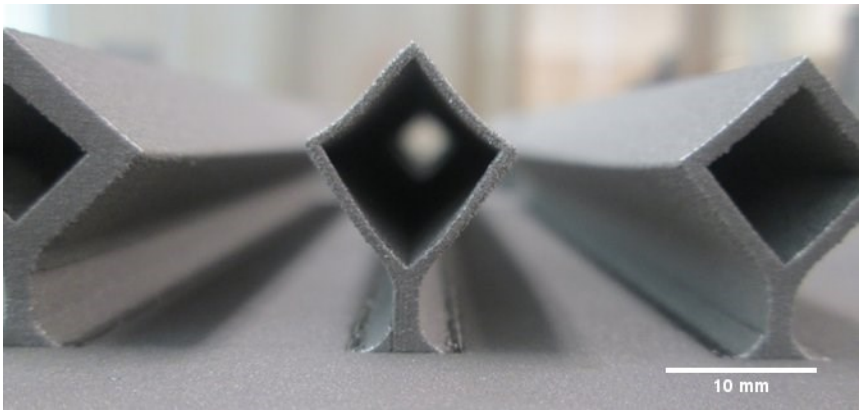

Figure 4-4: Aligned frontal view of a series of printed samples with varying wall thickness.

Deformations observed were negative at the ends (contraction) and positive at the center (swelling) creating an overall negative bending along length of the tubes. A number of studies confirmed that following separation from the supports and base plate, positive bending in z (i.e. normal to the base plate) occurs; this is characterized by distinct lifting of the corners and edges from the plate or supports due to the particular residual stress distribution caused primarily by cooling from the temperature gradient mechanism (TGM) (Figure 4-5b) [16, 57-60], while distortions during fabrication can be more complicated [17]. In terms of geometric features, it is also important to note that overhanging structures behave much differently than simple structures directly connected to the base plate due to the lack of immediate mechanical constraints except where support

structures are employed, and residual stress studies concerning these features are severely lacking [61].

The overall negative bending observed in this study prior to separation from the base plate is similar to the thermomechanical model proposed by M.F. Zaeh and G. Branner for deformations during fabrication and can be explained by the high thermal stress exceeding the yield strength of the material, thus causing bending of the structure away from the laser beam (Figure 4-5a) [17]. The thin, angled walls in this study will see a reduced rate of heat dissipation and thus a less significant temperature gradient during cooling than the bulk samples typically studied, which may explain the negative bending observed. The direction of bending may also be attributed to a warping behavior shown in the overhanging layers due to the reduced mechanical constraints from the previous layer [62].

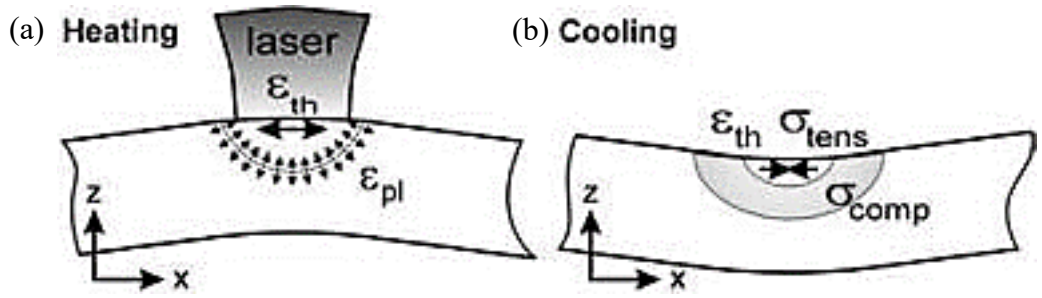

Figure 4-5: Drawing depicting the deformation mechanisms occurring by the TGM [10].

Figure 4-6 shows a graph of the average inelastic deformation occurring during fabrication measured for 9 of the primary specimens compared with the original CAD models, with length and wall thickness as variables. Results are plotted as average deformations at the center and ends separately in Figure 4-6a and c, and as total deformation (i.e. difference between center and ends) in Figure 4-6b and d. Where duplicate samples were available (i.e. 50.8 mm length tubes with 0.5mm, 1.0mm, and 2.0mm wall thickness), deformations were averaged between the two.

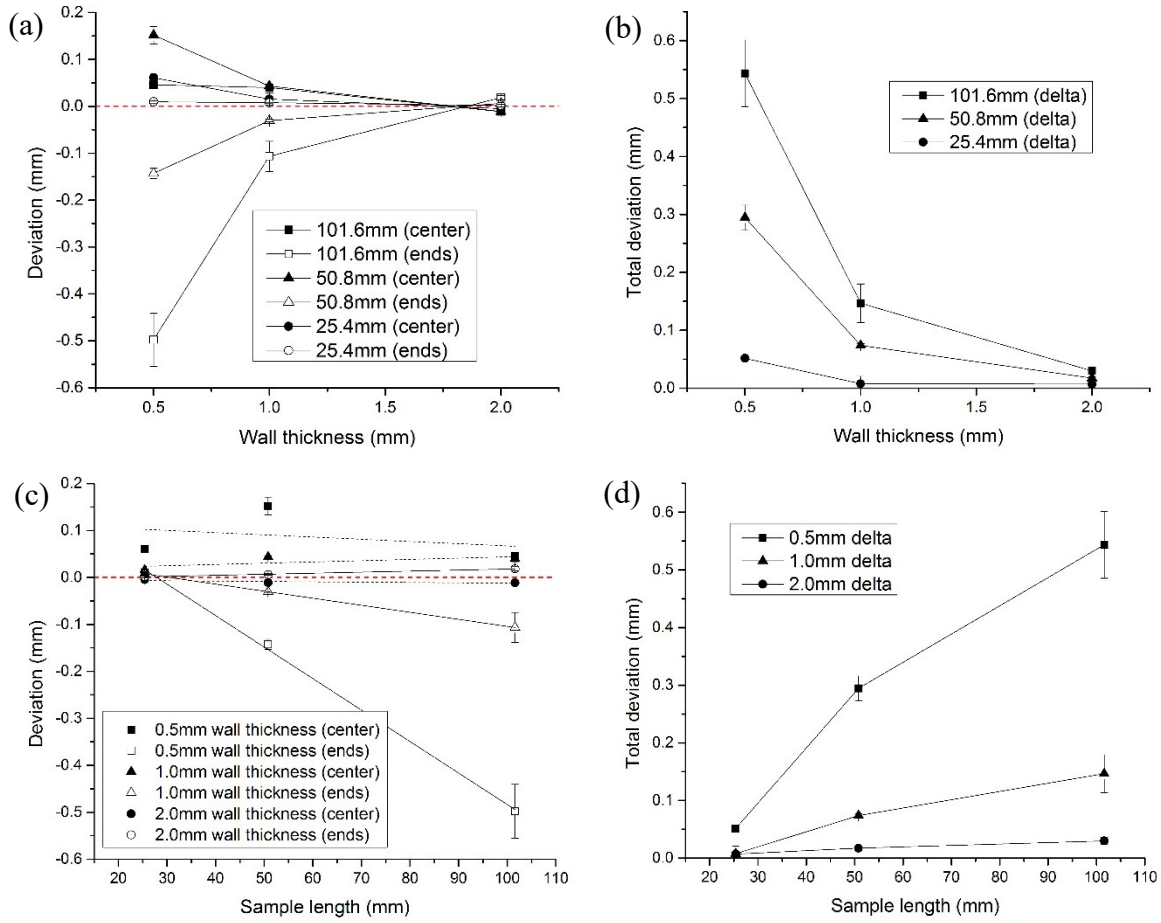

Figure 4-6: Average deformations as a function of wall thickness and sample length. Results displaying the relationship between deformation and wall thickness are plotted (a) by measurements taken at the ends and at the center of the samples and (b) as total (delta) deformation to eliminate alignment issues during CMM measurement. Results displaying the relationship between deformation and sample length are similarly plotted in (c) and (d).

The relationship between the average magnitude of the measured deformations and the wall thickness of the samples is shown to be non-linear, with maximum deformations obtained for the 0.5 mm thick specimen (Figure 4-6a and b). Conversely, the relationship between the average magnitude of deformations and the length of the samples appears to be approximately linear when isolating deformations at center and ends (Figure 4-6c). However, when plotting the total deformation (i.e. the sum of the absolute values of deformation measured at the center and ends of the specimen), the effect of length is shown to be non-linear (Figure 4-6d) and in fact suggests that its influence on deformations, while increasing, becomes less important as length increases.

Figure 4-7 through 4-9 show the top-down deformation measurements aligned with the original CAD drawings for the rectangular tubes with 45° overhang for varying length and wall thickness, allowing one to clearly see the deformation patterns observed. The distortion maps represent the geometric deviations from the intended dimensions (as provided in the CAD drawing) and are shown as magnitudes of a vector D equal to the sum of individual directional vectors D_x, D_y, and D_z, and adjusted for symmetry about the y-axis. The colour scale is kept uniform for all samples to properly illustrate and compare the distortions observed as a function of the given variables. The measured average deformations are presented in Table 4-2.

As expected, in all cases the samples with wall thickness of 2.0 mm exhibited minimal deformations, only exceeding 0.01 mm magnitude for the 101.6 mm long specimen, indicating that thermal stresses most likely did not exceed the yield strength of the material in the majority of the sample volume. As wall thickness was reduced, however, deformations became more apparent. Samples with a 1.0 mm wall thickness were considerably more distorted, with D_{avg} equal to more than 3 times the equivalent length of 2.0 mm wall thickness samples. Only in the case of the shortest 25.4 mm long specimen were deformations relatively insignificant. Finally, severe deformations (in excess of ±0.25 mm misalignment from the original design) were observed in the 0.5 mm wall thickness samples for lengths of 50.8 mm and greater, indicating very high residual stresses in large portions of the sample volume. Deformations in the shorter 25.4 mm length sample were significantly lower (<0.10 mm), though still apparent compared with samples of identical length and greater thickness.

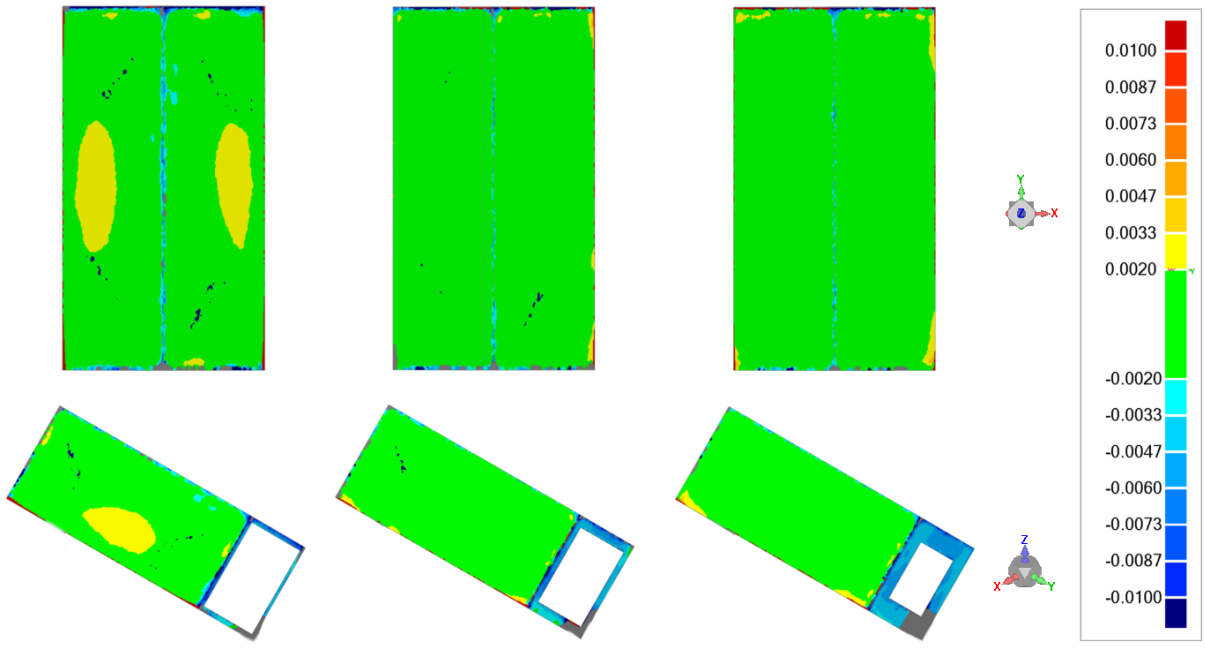

Figure 4-7: Distortion maps (in inches) from the metrology alignments of 25.4mm length rectangular tubes with (from left to right) wall thicknesses of 0.5mm, 1.0mm, and 2.0mm prior to separation from the base plate.

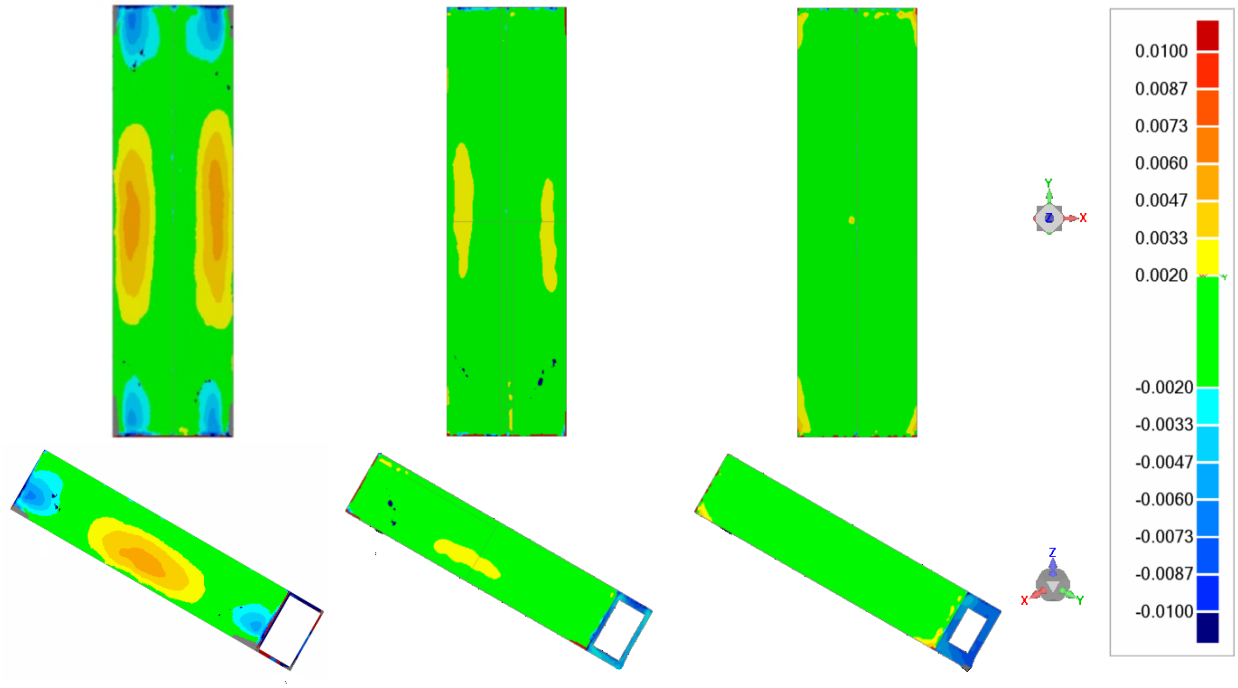

Figure 4-8: Distortion maps (in inches) from the metrology alignments of 50.8mm length rectangular tubes with (from left to right) wall thicknesses of 0.5mm, 1.0mm, and 2.0mm prior to separation from the base plate.

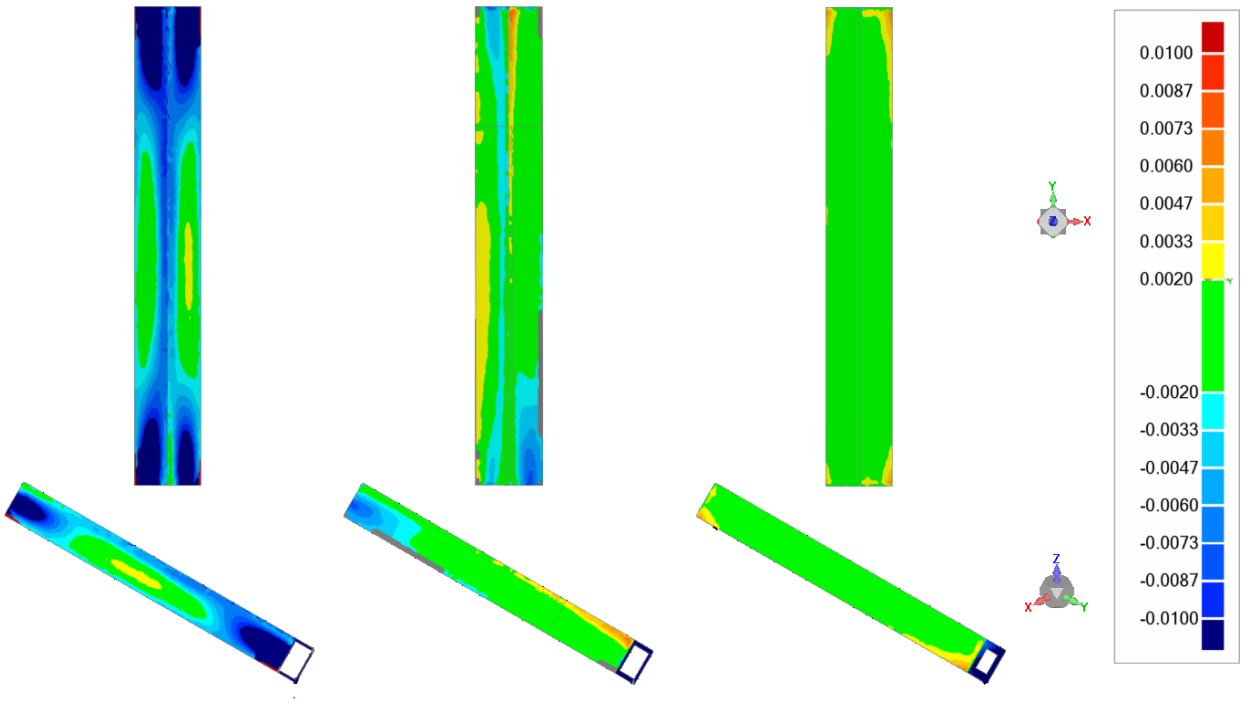

Figure 4-9: Distortion maps (in inches) from the metrology alignments of 101.6mm length rectangular tubes with (from left to right) wall thicknesses of 0.5mm, 1.0mm, and 2.0mm prior to separation from the base plate.

Table 4-2: D_{avg} measured for the 9 specimens with varying wall thickness and length.

Wall thickness (mm)	**Sample length (mm)**	***D_{avg}* (mm) measured at the center**	***D_{avg}* (mm) measured at the ends**	***ΔD (mm)***
0.5	25.4	0.061 ± 0.003	0.010 ± 0.003	**0.051 ± 0.004**
0.5	50.8	0.152 ± 0.019	-0.143 ± 0.011	**0.294 ± 0.021**
0.5	101.6	0.046 ± 0.008	-0.498 ± 0.057	**0.544 ± 0.058**
1.0	25.4	0.015 ± 0.013	0.008 ± 0.001	**0.008 ± 0.013**
1.0	50.8	0.043 ± 0.002	-0.030 ± 0.003	**0.074 ± 0.003**
1.0	101.6	0.040 ± 0.008	-0.107 ± 0.032	**0.147 ± 0.033**
2.0	25.4	-0.005 ± 0.000	0.002 ± 0.003	**0.007 ± 0.003**
2.0	50.8	-0.011 ± 0.002	0.006 ± 0.002	**0.017 ± 0.002**
2.0	101.6	-0.011 ± 0.004	0.018 ± 0.004	**0.030 ± 0.006**

Figure 4-6a and b show deformations as a function of wall thickness. The wall thickness influences the heat flow (and by extension the magnitude of residual stresses generated) as well as the sample's ability to mechanically resist the effects of a given amount of internal stress. From a

mechanical standpoint, greater wall thickness affects both the immediate generation of thermal and residual stresses and the ability of the structure to withstand deformations on a layer-by-layer basis. Timoshenko proposed an equation for estimating the curvature κ of bimetal strips subjected to uniform heating (Equation 4-1), where α is the coefficient of thermal expansion (CTE), I is the area moment of inertia (given in Equation 4-2, where x is the layer width), h is the thickness of the strip, and E is the elastic modulus [63]. By adapting this equation to AM, similarly to that proposed by Amon et al. [64], Equation 4-3 can be obtained wherein α, I, h, and E can be considered identical for two subsequent layers.

$$\kappa = \frac{(\alpha_2 - \alpha_1)(T - T_0)}{\frac{h_1 + h_2}{2} + \frac{2(E_1 I_1 + E_2 I_2)}{h_1 + h_2}\left(\frac{1}{E_1 h_1} + \frac{1}{E_2 h_2}\right)} \tag{4-1}$$

$$I = \frac{x h^3}{12} \tag{4-2}$$

$$\kappa = \frac{\alpha \Delta T}{h + \frac{2EI}{h}\left(\frac{2}{Eh}\right)} \tag{4-3}$$

From this equation, it would appear that the layer width x (and thus wall thickness) would linearly affect deformation during fabrication. However, this equation only considers deformations occurring in the vertical z-axis, where in reality the deformation vectors measured are nearly perfectly normal to the tube wall. Therefore the area moment of inertia would reflect the rotated nature of the tube geometries and would be proportional to t^3, where t is the geometric wall thickness.

It can also be expected that the wall thickness will directly affect the temperature gradient observed. The following differential equation describes the 3D heat conduction occurring during LPBF:

$$\rho \frac{\partial (C_p T)}{\partial t} = \frac{\partial}{\partial x}\left(K \frac{\partial T}{\partial x}\right) + \frac{\partial}{\partial y}\left(K \frac{\partial T}{\partial y}\right) + \frac{\partial}{\partial z}\left(K \frac{\partial T}{\partial z}\right) \quad (4\text{-}4)$$

where ρ is density, C_p is the heat capacity, t is time, and K is the material's thermal conductivity, with the following boundary condition:

$$K \frac{\partial T}{\partial n} + h(T - T_0) + \sigma\varepsilon(T^4 - T_0^4) = q \qquad (x, y, z) \in S \quad (4\text{-}5)$$

where n is the normal vector of surface S, h is the heat convection coefficient, T_0 is ambient temperature, σ is the Stefan-Boltzmann constant, and ε is the emissivity of the material [65]. Theoretically, heat is conducted uniformly in all directions; however, heat conduction occurs much less rapidly through the surrounding powder than through the volume of the bulk metal [66, 67]. A reduced wall thickness will cause the isolating effects of the surrounding powder to be more significant, potentially causing higher thermal gradients to develop during heating (initial TGM contribution) coupled with a slower cooling rate from the more restricted heat dissipation. Conversely, a greater wall thickness and thus greater sample volume will exhibit a greater cooling rate, balancing the initial distortion contribution of the TGM while causing more significant residual stresses to develop. However from the observed deformations, it is clear that the increase in mechanical stiffness from the added wall thickness greatly contributes to the specimen's ability to withstand geometric deformation due to these high thermal stresses.

From Figure 4-6c and d, deformations are shown to be greater with increased sample length. Though the overall trend is more linear than that of the wall thickness, the effect does appear to diminish slightly as length increases (Figure 4-6d). The length scales studied are an order of magnitude greater than the sample thickness. Furthermore, from thermal simulations conducted on CP-Ti powder during LPBF, the temperature gradients are observed to be highest in an area very close to the laser, quickly dropping off at greater distances (~1.0 mm) [68]. Along the tube

lengths considered, differences in temperature gradient are expected to be minor between the 3 cases when holding all other variables constant, and becoming less important at greater sample lengths. In terms of mechanical resistance, because distortions did not occur in the direction parallel to the length of the tube samples, the length variable does not contribute to the specimen's area moment of inertia. Nonetheless, a specimen with increased length will exhibit greater deflection due to a reduction in bending stiffness. Mathematical models have been proposed by T. Wang et al. and supported by Z. Zhu et al. which include the section length of a layer as an important parameter affecting the magnitude of deformations in fused deposition modelling (FDM) using a simple rectangular geometry [69, 70]. The model proposed by Z. Zhu et al. for AM of a polymer structure is shown in Equation 4-6, where s is the distortion observed, N and n are the number of layers built and being deposited respectively, α is the CTE, T_g and T_r are the glass transition temperature and room temperature respectively, t is the layer thickness, and L_s is the length of the layer [70].

$$s = \frac{(N+n)^3 t}{6\alpha N(T_g - T_r)}\left[1 - \cos\left(\frac{3\alpha N L_s}{(N+n)^3 t}(T_g - T_r)\right)\right] \tag{4-6}$$

4.3.2. Geometric distortions as a function of the angle of overhang

Figure 4-10 show the top-down metrology alignments of the two samples built with greater angle of the walls (defined here as greater angle to the horizontal and thus reduced degree of overhang). The samples have identical length and wall thickness; however, due to the increased angle of the walls, the aspect ratio of the samples will differ. The negative bending direction can again be seen for these samples. Moreover, from the alignments a trend in the magnitude of measured deformations can clearly be identified. The sample built with the greatest angle to the horizontal

also suffered the greatest distortions. The measured average deformations are plotted in Figure 4-11.

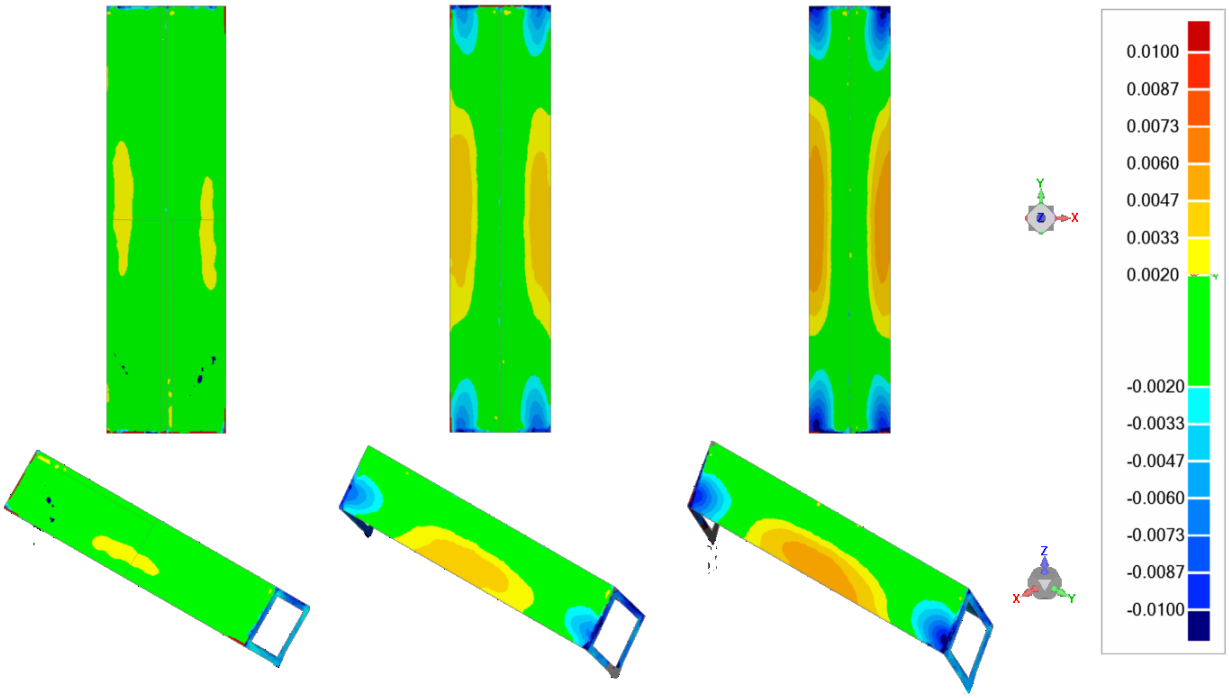

Figure 4-10: Distortion maps (in inches) from the metrology alignments of three rectangular tubes built with varying angles of overhang. From left to right, the angles of overhang are 45º, 54º, and 63º. All sample have identical length (50.8mm) and wall thickness (1.0mm).

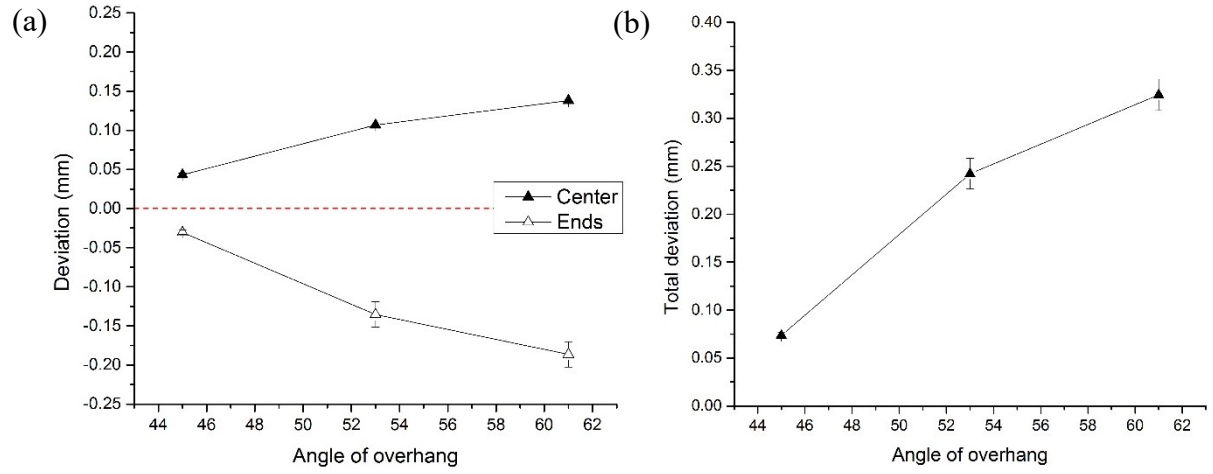

Figure 4-11: Average deformations as a function of the angle of overhang. Deformations are plotted (a) independently at center and ends of the specimens and (b) as total (delta) deformations in order to eliminate alignment issues during CMM.

To date, the effect of overhanging features remains a relatively poorly studied area, with most published research focused on the reduction in build quality for angled parts due to the staircase effect and balling owing to the increased interaction area with the surrounding powder [61] [62, 71]. In terms of heat transfer, the isolating effect of the surrounding loose powder for a structure with more overhanging material per layer will act as an important barrier to heat conduction, causing an increase in heat residence time and melt pool volume, hence why support structures are often employed at these critical angles [71]. Thus it would be expected that a smaller overhang angle would cause a noticeable decrease in surface quality, but may also cause greater initial temperature gradients to develop locally within the overhanging region due to overheating, as well as a reduced cooling rate compared with a higher angled structure. Due to the overhanging material being unconstrained, this results in a distinctive upwards warping due to the elevated thermal stresses. However, this warping is limited to the overhanging material in each layer and is not known to have a noticeable effect on the bulk structure at the angles studied [62]. Moreover, when observing the outer surface of the specimens, it is clear that the higher angled structures suffered the greatest distortions. This trend is likely influenced by other aspects of the specimen geometry which changed as a result of the differing angle of overhang.

From the design of the specimen, minor differences exist in the thickness of the walls in the horizontal x-axis as perceived during a single layer. When isolating a single layer of the process, the layer width, which in this case is a function of both the geometric wall thickness and the angle of overhang, will decrease with increasing angle (Table 4-3). Though the difference is small (~0.27 mm from 45° to 61°) this may cause a slight reduction in mechanical stiffness for a given layer.

Table 4-3: Layer width calculated for three different angles of overhang with constant geometric wall thickness of 1mm.

Angle of overhang	Layer width (mm)
45°	1.414
53°	1.252
61°	1.143

A second contribution which likely explains the greater observed distortions at higher angles of overhang is the height of the sample, or more specifically the number of layers. Since the surface areas of the walls were held constant and only the angle of overhang was modified from one sample to the next, samples built with a greater angle of overhang will have an increased total height and thus will require more layers to fabricate. The 53° and 63° geometries require 12.9% and 23.7% more layers respectively to fabricate than the 45° geometry. It has been shown in the literature that increasing the number of layers in LPBF causes greater residual stresses to develop up to a certain point due to the compounding nature of residual stress accumulation in this process, where each added layer will cause greater tensile stresses at the top of the structure and compressive stresses at the bottom [10, 28], increasing the susceptibility for material yielding. Furthermore, reduced heat conduction into the build plate for each subsequent layer causes higher temperatures to develop, thus yielding greater thermal gradients during heating [55].

4.3.3.Measurement of relaxation distortions

To further quantify residual stress induced deformations in LPBF, it is important to measure distortions arising from the relaxation of said residual stresses upon separation of the samples from the base plate. The base plate as well as the thin single support used in this case act as stiffening elements during the process. Once the stiffening elements are removed, the stresses at and around the sectioning plane are free to relax, acting as a second source for deformations in LPBF [10, 17].

Typically, a stress relief heat treatment specific to the material in question is employed to eliminate residual stresses prior to separation from the base plate.

Table 4-4 shows a comparison of average deformations measured following removal from the base plate on the reference samples which were stress relieved prior to removal and on the as built samples with identical geometries. As expected, all samples subject to the stress relief heat treatment per AMS 2801 showed little to no further deformations following removal from the base plate and thus its effectiveness here is confirmed. For samples which were not heat treated prior to removal, non-negligible deformations were measured. In the case of the 0.5 mm thick specimen, complete sample failure was observed; the tube split open along its length near the support structure. For both the 1.0 mm and 2.0 mm thick specimens, values of *D* were measured below 100 µm. Interestingly, in the case of the 2.0 mm thick specimen, distortions caused by relaxation were more significant than those arising from the fabrication process itself. During fabrication, specimens with 2.0 mm wall thickness showed little to no deformations from heat input, which can be attributed to the fact that these samples had much greater mechanical constraints preventing these immediate distortions. However, due to the principal of TGM in residual stress generation, this likely means that a greater magnitude of residual stresses remain in the part which can cause distortions upon separation from the base plate.

After removing the samples from the base plate, all samples which exhibited further deformations showed the “peeling up” behavior characteristic of residual stress relaxation in LPBF specimens where the edges of the samples are lifted upwards (positive bending) [57, 58].

Table 4-4: Comparison of average deformation magnitude in reference (stress relieved) and as built samples following removal of the specimens from the base plate.

		D (mm) after separation from the base plate	
Specimen length (mm)	Specimen thickness (mm)	Stress Relieved	As Built
50.8	0.5	<0.010	Specimen failure
50.8	1.0	<0.001	~0.017
50.8	2.0	<0.010	~0.083

4.3.4. Residual stress measurements

Residual stress measurements were performed following removal from the base plate to accommodate the chamber size of the diffractometer. Figure 4-12 shows the locations where residual stress measurements were taken on the sample of length 50.8 mm and wall thickness 0.5 mm. The results are shown in Table 4-5. For comparison, one measurement was taken in the center of one edge on a sample of length 50.8mm and wall thickness of 2.0mm is also presented in Table 4-5. The stresses recorded were all tensile in nature since these were taken at the top surface of the specimens. From the literature, it is known that in LPBF residual stress generation is highly tensile at the top layers [10].

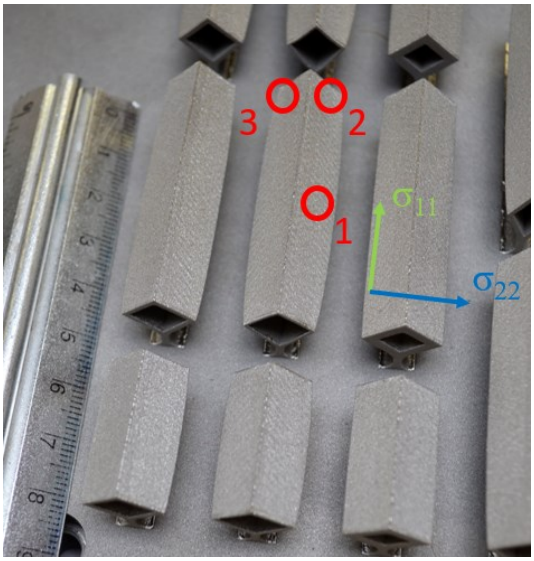

Figure 4-12: 3 key areas examined for residual stresses by XRD for a rectangular tube sample with length of 50.4mm and wall thickness of 0.5mm.

Table 4-5: Residual stress measurements on a select set of samples.

Sample length (mm)	Wall thickness (mm)	Area	σ_{11} (MPa)	σ_{22} (MPa)
50.8	0.5	1	438 ± 188	630 ± 130
		2	684 ± 187	613 ± 128
		3	879 ± 238	756 ± 164
50.8	2.0	1	950 ± 199	793 ± 135

Comparing residual stresses measured in corresponding areas on the 50.8 mm long samples with wall thicknesses of 0.5 mm and 2.0 mm respectively, it can be seen that the magnitude of the remaining residual stresses in the untreated 2.0mm thick specimen is greater than those in the 0.5mm thick specimen, supporting the observations made during removal from the base plate.

4.4. Conclusions

From the above study, the following general statements can be made which may act as practical guidelines to follow to avoid irreparable damage or unnecessary added costs when producing components using a high energy density AM method:

- Negative bending in z was observed in the top portion of the specimens, which indicates that deformations owing to thermal stresses occurred during the initial heating stage of the TGM causing rapid expansion of the topmost layer. This can likely be attributed to reduced heat dissipation caused by the overhanging features of the specimens as well as warping of the overhanging material in each layer.
- Wall thickness had a non-linear impact on the magnitude of deformations. Increasing the thickness of the walls drastically reduced deformations due to the greatly increased

mechanical resistance of the structure. At a wall thickness of 2.0 mm, deformations were insignificant for all sample lengths.

- Isolating the length of the tubes as a variable showed increasing deformations with sample length as expected, though the trend appeared to become less important at greater lengths suggesting a diminishing effect of this variable.
- The angle of overhang represents a complex variable with situational effects that may require further study. In the present study, the angle of the component wall indirectly influences the magnitude of deformations measured due to process-induced thermal stresses. This can likely be attributed to a slight reduction in mechanical stiffness for higher angled structures as well as an increase in the total number of layers required to produce the component.
- No deformations were present in the stress relieved specimens following separation from the base plate, indicating that the heat treatment selected was appropriate. Conversely, further deformations were observed in the built samples due to relaxation of the residual stresses upon separation. For an identical length, the 2.0 mm thick sample showed greater relaxation than the 1.0mm thick sample indicating greater residual stresses present in the former. Surface residual stress measurements support this observation. Complete specimen failure was observed for the 0.5mm thick as built sample upon separation. In all cases where relaxation occurred, a positive bending direction was observed typical of relaxation of residual stresses in AM suggesting that the distribution of longitudinal residual stresses along the z axis within the specimens was similar to those expected in simple structures.

4.5. Acknowledgements

The authors acknowledge the help of Liburdi for assistance with CMM measurements and Edmit Industries for sample manufacturing. The authors also acknowledge CRIAQ and industrial sponsors GE Aviation, Bell Helicopter, MDA, Héroux Devtek, CMQ, PWC, CLS, and Bombardier Aerospace for support.

Chapter 5 – Relationship between Microstructure and Dilatation Response during Thermal Cycling for Ti6Al4V Fabricated by Laser Powder Bed Fusion

Preface

Relationship between Microstructure and Dilatation Response during Thermal Cycling for Ti6Al4V Fabricated by Laser Powder Bed Fusion is a comprehensive study, the results, conclusions, and procedures of which are detailed in Chapter 5. This article is intended for publication in the year 2018 and presents findings related to the effects of design and process conditions in Laser Powder Bed Fusion on the coefficient of thermal expansion in Ti6Al4V. Below is the expected citation for the article:

J. Danovitch, J. Choi, J. Mezzetta, L. Nguyen, N. Chekir and M. Brochu. *Relationship between microstructure and dilatation response during thermal cycling for Ti6Al4V fabricated by laser powder bed fusion*. *Article intended for publication.* 2018

Abstract

This study provides an understanding of Ti6Al4V fabricated by laser powder bed fusion regarding the effects of build direction and the resulting microstructure on the linear rate of thermal expansion. Anisotropic behavior of the linear thermal expansion was observed depending on build direction (X, 45^{o}, Z) and influenced by the heat treatment applied (stress relief, mill anneal and hot isostatic pressing). Thermal stability was found to be approximately equal for the mill annealed and HIP conditions, while stress relieved samples were found to be noticeably less stable. Finally, thermal cycling as a possible source of residual stress development in AM parts was investigated, but was found through XRD analysis to be an insignificant source.

KEYWORDS: Ti6Al4V, microstructure, additive manufacturing, powder bed fusion, anisotropy, thermal expansion

5.1. Introduction

Additive manufacturing (AM) processes, in particular laser-based processes such as laser powder bed fusion (LPBF), offer a degree of customizability that is unique when compared with conventional processing routes. In terms of materials used in AM, Ti6Al4V, a weldable α-β titanium alloy with a high strength to weight ratio, is one of the workhorse alloys for the adoption of this new manufacturing technology [1]. In aerospace, this alloy is typically used either as an airframe material or more commonly in the low temperature regions of the gas turbine engine [3]. Due to the heat generated by the gas turbine engine, extensive thermal cycling is expected to occur over the lifetime of the component. As such it becomes important to understand the thermal behavior of additively manufactured Ti6Al4V to validate if phenomenon degrading the properties of the component might occur. Specifically, the accumulation of residual stresses [48, 72], the onset of thermal fatigue from a high number of thermal cycles [48], and improperly considered tolerances of the component could cause the component to function improperly or to eventually fail [52]. This is of paramount importance considering the existing anisotropy in AM parts created by the columnar grain structure [15, 73].

To date, no work on thermal cycling experiments conducted on Ti6Al4V coupons fabricated by LPBF was found. The present study was initiated on the premise of work performed on wrought components, where the focus of these studies was to determine the thermomechanical response of the alloy given specific sets of heating and cooling rates with varying temperature ranges [46-49]. M.N. Mungole et al. reported an initial increase in strength to 1150MPa and decrease in ductility to 7% after 50 cycles from RT to near-beta-transus temperatures (950^{o}C) followed by a loss in

strength down to 540 MPa after 100 cycles due to the appearance of an initially finer microstructure with approximately 50% β content which transformed into a coarser network of α-β platelets with reduced β (35%) [50]. In this same study, a decrease in strength (500 MPa) followed by a subsequent increase (1200 MPa) with little to no reported loss of ductility for cycling up to 875 ºC was observed, owing to the evolution of a very fine needle-like microstructure after 50 cycles followed by a return to the coarser basket weave structure from 100 cycles onwards. Additional cycles at this same temperature range saw a return to the original pre-cycling strength with a finer lamellar microstructure.

In terms of dilatometry, very few thermal analyses involving this alloy were conducted and to the authors' knowledge, none of these were performed over several cycles; instead they focused on single heating/cooling segments with varying temperature ranges and/or heating and cooling rates with the purpose of identifying phase changes. In a study by P. Homporová et al. [34], dilatometric experiments up to 1100 ºC were performed on samples which had been heated up to temperatures in the α+β range (~930 ºC) and then subjected to various cooling rates to obtain different starting microstructures. A delay in the rate of linear expansion was observed above 750 ºC attributable to the primary α→β transformation. This was shown to be far more pronounced for samples which had been air cooled or furnace cooled, both of which had a greater primary α content in their starting microstructure. A second, slighter delay was shown around 450ºC for the water quenched sample and to a lesser degree the air cooled sample attributable to the α'→α transformation. Other studies conducted such experiments at temperatures far exceeding those of import in this report which focuses on temperatures at and slightly above the expected operating temperature of Ti6Al4V in typical aerospace applications [35, 36, 74].

The present work focuses on measuring the thermal dilatation response of Ti6Al4V components built by LPBF when subjected to a series of thermal cycles under different temperature ranges to simulate aerospace applications subjected to thermal cycling. The dilatometric curves will be examined to determine the stability of the components during these thermal cycles as well as to obtain values for the coefficients of thermal expansion as a function of build direction (prior beta grain orientation) and post-processing heat treatment.

5.2. Experimental Procedure

The AM samples were fabricated by LPBF using a Concept Laser M2 Cusing unit using standard building parameters for Ti6Al4V with spherical Ti6Al4V ELI grade 23 powder as supplied by the machine manufacturer. The laser scanning pattern used was the 'island scanning' strategy [17]. The particle size distribution was specified by the manufacturer to be in the range of 20 – 50 μm and was confirmed in a previous study using a Horiba Laser Diffraction Particle Analyzer [15]. The impurity limits of the as-received powder as listed in the supplier data sheet is shown in Table 5-1. Oxygen content was confirmed to be within the allowable tolerance by the LECO 834 inert gas fusion technique, yielding 0.11 wt%. Samples were built in three different build orientations: laid flat horizontally (*X-direction)*, upright vertically (*Z-direction)* and at an angle of 45°.

Table 5-1: Alloy composition of the grade 23 Ti6Al4V ELI powder provided by the supplier.

	Impurity Limits (wt% max)				
AMS 4907 ELI Ti6Al4V	N	C	H	Fe	O
	0.05	0.08	0.012	0.25	0.13

All samples were stress relieved according to the AMS 2801 standard [56] following fabrication in order to prevent geometric deformations of the samples upon removal from the base plate. Selected samples for each of the three build directions (x, z, and 45°) were then mill annealed according to the AMS 2801 standard [56]. A separate subset of samples from each of the three build directions were subjected to hot isostatic pressing (HIP) within the range specified in the ASTM F2924 standard [75]. Following heat treatment, the samples were machined to the specifications required by the dilatometer (cylinders with a diameter of 3 mm and a height of 10 mm).

Microstructural observations were carried out on samples having been prepared using typical metallographic procedures with a final polishing step on colloidal silica using a Vibromet. Density assessment on the initial samples was performed in a previous study by optical microscopy using a Clemex microscope and subsequent image analysis using the Clemex Professional Edition software on the polished cross sections [15]. Microstructural examination was performed on samples which have been etched using Kroll's Reagent containing 2% hydrofluoric acid (HF), 6% nitric acid (HNO3) and 92% distilled water for 20 seconds

The evaluation of the deformation during thermal cycling was assessed using a Linseis L78 R.I.T.A. Quenching Dilatometer. Cylindrical specimens of 10mm in height by 3 mm in diameter were used; samples extracted by electrical discharge machining (EDM) from the 9 build

orientations/heat treatment conditions described above. The dilatometer was equipped with fused silica pushrods with near-zero coefficient of thermal expansion (CTE) and was operated under a prepurified helium (99.995% purity) shielding environment. Two test regimes were investigated. The first was set between 25 and 750 ºC using heating and cooling rates of 27 and 16 ºC/sec respectively, and a holding time of 5 minutes at the maximum and minimum temperatures. This upper temperature limit represents an extreme case and is atypical of this alloy for engine applications, while heating and cooling rates were chosen to approximate conditions found in sections of the fan and compressor, where Ti6Al4V is most often used [3]. This set was used for all combinations of build direction and heat treatment. A second set of tests were performed between 25 and 400 ºC, below the expected major microstructural transformations in Ti6Al4V the same heating and cooling rates as the first set of tests again with 5 minute holding time. Due to the results obtained for the initial set of thermal cycles, stress relieved specimens were ignored in this scenario. This second upper temperature limit was chosen as it approximates the typical maximum operating temperature of this alloy in the fan and compressor regions [3, 37, 38]. Both cycling regimes were performed for 50 continuous cycles for each sample.

The linear coefficient of thermal expansion (CTE) as a function of temperature and/or time (i.e. over the course of the set number of cycles) can be calculated from the measured change in length using equations (5-1) and (5-2):

$$\alpha(T) = \frac{de_T}{dT} \tag{5-1}$$

$$\bar{\alpha}(T) = \left(\frac{1}{T - T_{ref}}\right) e_T(T) \tag{5-2}$$

where α and $\bar{\alpha}$ are the linear CTE and average linear CTE respectively, T and T_{ref} are the measured temperature and reference temperature respectively, and e_T is the thermal strain and is expressed in equation (5-3):

$$e_T(T) = \frac{\Delta L_{thermal}}{L} \tag{5-3}$$

where $\Delta L_{thermal}$ is the change in length of the sample due to thermal sources and L is the original length of the sample prior to thermal cycling [76].

Scanning electron microscopy (SEM) was performed using a Hitachi SU3500. Electron back-scattered diffraction (EBSD) analysis was also performed on the SEM in order to examine crystallographic orientation and texture of the various specimen using Oxford Instruments-HKL Channel 5 software. Map sizes of 500 µm x 500 µm were taken, using a step size of roughly 0.2µm for high resolution acquisition. Reconstruction of the β phase was carried out by following the Burgers orientation relationship $(0001)_\alpha//(110)_\beta$ and $\langle 11\bar{2}0\rangle_\alpha//\langle 111\rangle_\beta$.

X-ray diffraction (XRD) was performed using a Cu-source Bruker D8 Discover (k_α = 1.5418 Å) unit in order to determine phase composition, from which lattice expansion measurements were calculated, as well as to measure residual stresses prior to and following high temperature thermal cycling. Biaxial 2-dimensional residual stresses were measured on the α-Ti 112 peak from 2θ =75.00° to 76.90°. A pseudo-Voigt profile lineshape function was used to obtain values for residual stresses from the diffraction pattern.

5.3. Results and Discussion

5.3.5. Microstructure

Prior to thermal cycling, initial microstructures were examined and correlated with previously documented results to properly understand the factors that might affect the thermal behavior of each sample. Figure 5-1 shows optical micrographs of the different build directions to highlight the prior-β grain morphology. Columnar prior-β grains were measured at 272 ± 104 µm in length by 50 ± 16 µm in width for all sample conditions, growing in the direction of the incident laser beam during the LPBF process. Within these regions, as shown by the optical micrographs in Figure 5-2, elongated α (α/α' in the case of stress relieved and mill annealed conditions) platelets are present. Slight coarsening of the α phase has been previously reported in the mill annealing and HIP conditions, with the greatest degree of coarsening visible in the HIP microstructure (from 10.5 ± 2.7 µm in length by 1.0 ± 0.6 µm in width for the stress relief to 12.5 ± 3.5 µm by 2.0 ± 0.8 µm following mill annealing and 12.8 ± 4.0 µm by 3.2 ± 0.6 µm following HIP) [13, 15]. Microstructures of LPBF fabricated Ti6Al4V samples are well documented, and those obtained in this study are in agreement with available literature [15, 29, 77-79].

The extremely high cooling rates inherent to the LPBF process are known to yield a completely martensitic α' microstructure in Ti6Al4V devoid of any remaining β [13, 18, 29, 78]. Figure 5-2 shows higher magnification optical micrographs of samples subjected to each of the three heat treatments studied. The differences in the morphology of the α phase with heat treatment reported elsewhere are visible here [13]. The temperature of the stress relief heat treatment was very likely insufficient to initiate α'→α transformation, and so the microstructure is expected to be nearly identical to that in the as-built state i.e. an entirely martensitic microstructure. Available literature has confirmed that mill annealing is performed at a sufficiently high temperature to cause a partial

α'→α+β transformation while HIP produces an α-dominated microstructure with greater β phase formation [13, 15]. The absence of β phase in the stress relieved condition and the presence of β in the HIP condition have been confirmed by XRD analysis in Figure 5-3. S. Leuders et al. (2013) have shown the formation of β following a similar annealing heat treatment suggesting that a small amount of β is likely to be present in this case as well. For the HIP sample, β volume fraction could be measured at approximately 3% and appears at the boundaries of the α plates [15].

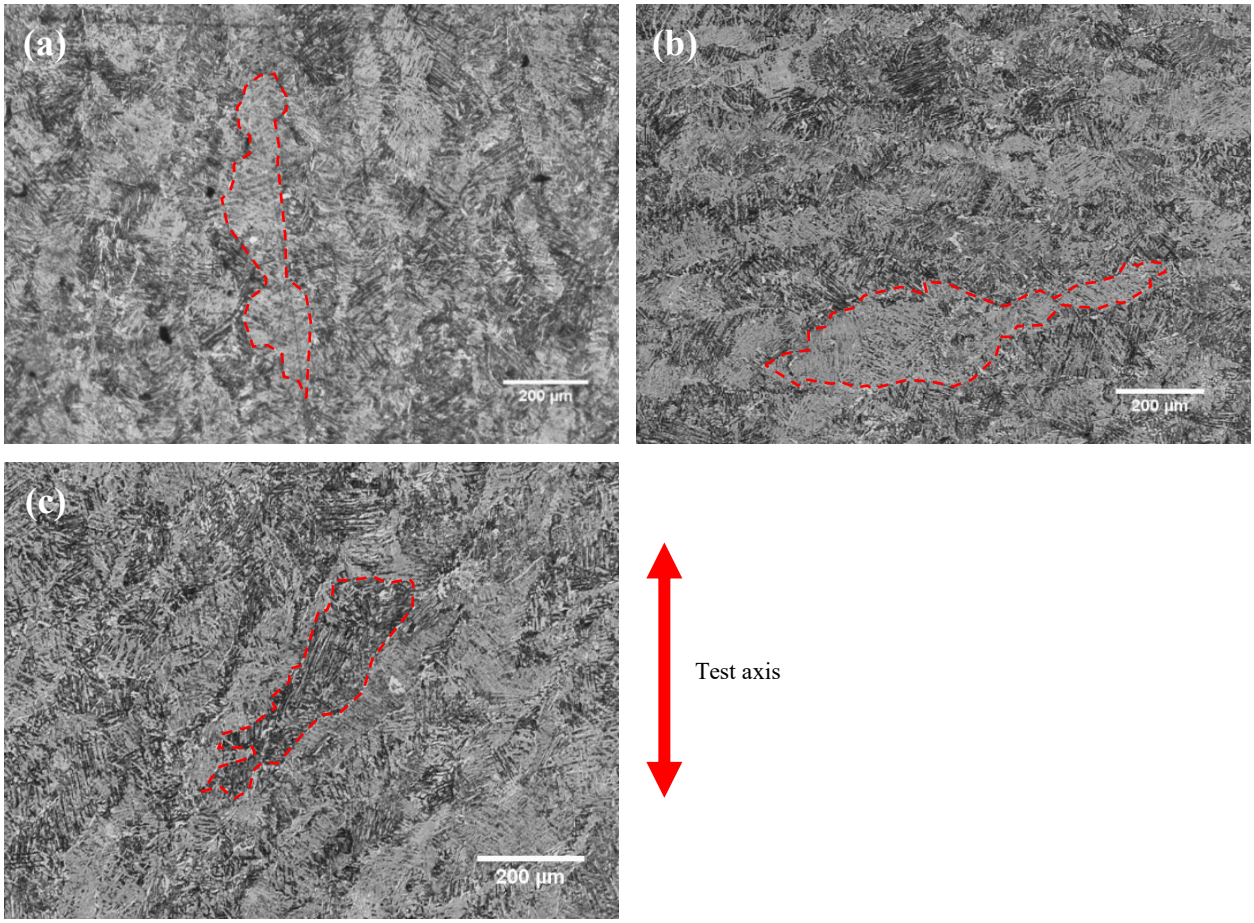

Figure 5-1: Optical micrographs showing the orientation of the elongated prior-beta regions with respect to the test axis for (a) a Z-direction HIP sample, (b) an X-direction HIP sample, and (c) a 45° HIP sample. For the current study, the naming convention is chosen such that samples built in the Z-direction have prior-β grains oriented parallel to the test axis, samples built in the X-direction have prior-β grains oriented perpendicularly to the test axis and samples built at 45° have prior-β grains oriented at an angle of 45° to the test axis.

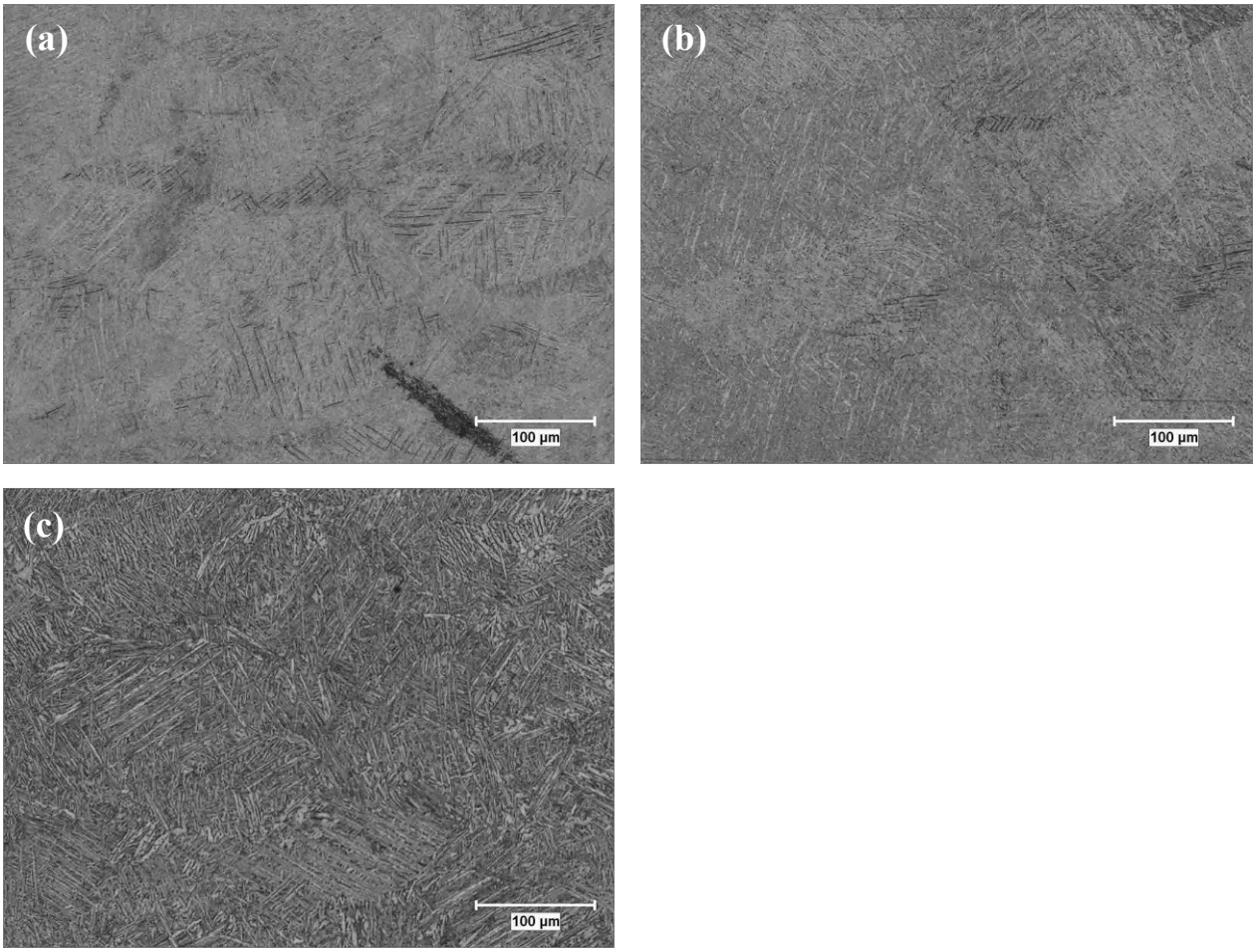

Figure 5-2: Optical micrographs showing the microstructures observed in each of the three heat treatments considered: (a) stress relief, (b) mill annealing, and (c) HIP.

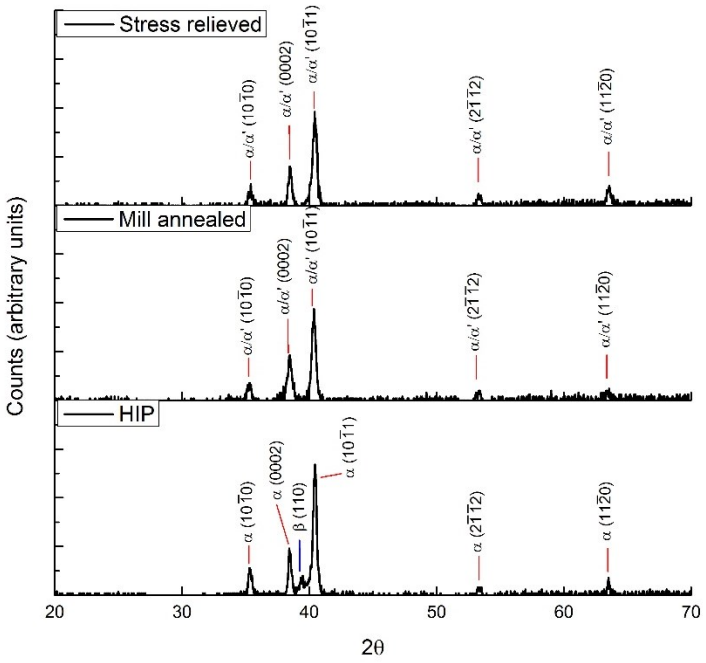

Figure 5-3: XRD scan patterns of samples built in the X-direction in the stress relieved, mill annealed, and HIP conditions.

5.3.6. Thermal cycling experiments

Room temperature to 750°C

Dilatometry curves for the high temperature cycling regime (RT to 750°C) are presented in Figure 5-4. Additionally, Table 5-2 shows the maximum linear CTE averaged over 50 cycles for all nine sample conditions. Linear expansion of the *X-direction*, *Z-direction*, and *45°* samples in the stress-relieved condition averaged at $\alpha_X = 12.8x10^{-6} \pm 0.19$ *m/m°C*, $\alpha_Z = 12.9x10^{-6} \pm 0.11$ *m/m°C* and $\alpha_{45} = 12.6x10^{-6} \pm 0.22$ *m/m°C* respectively over 50 cycles. For the mill-annealed condition, linear expansions were measured at $\alpha_X = 11.4x10^{-6} \pm 0.04$ *m/m°C*, $\alpha_Z = 13.1x10^{-6} \pm 0.11$ *m/m°C* and $\alpha_{45} = 12.8x10^{-6} \pm 0.12$ *m/m°C* and finally, linear expansion for samples in the HIP condition were measured at $\alpha_X = 11.4x10^{-6} \pm 0.04$ *m/m°C*, $\alpha_Z = 13.8x10^{-6} \pm 0.11$ *m/m°C* and $\alpha_{45} = 12.6x10^{-6} \pm 0.04$ *m/m°C*. Anisotropy between the three build directions is evident in the mill-annealed and HIP conditions. Conversely, no evidence of expansion anisotropy was noticed for samples in the stress-

relieved condition. From the literature, the thermal expansion of the HCP Ti-α lattice is known to be anisotropic [41, 42, 44, 45]. S. Malinov et al. (2002) determined through a series of synchrotron diffraction experiments at 1000 ºC that expansion along the prismatic direction (*c*) is greater than along the basal direction (*a*) for α-Ti as is typical for HCP structures in general [45]. However, an earlier study by R.R. Pawar and V.T. Deshpande (1968) suggested the inverse according to lattice expansion measurements performed up to 155 ºC [44]. This is further expanded upon by V. Nizhankovskii et al. (1994) and more recently by P. Souvatzis et al. (2007) where the proximity to an electronic topological transition is used to explain the expansion being greater along the basal direction at low temperatures [41, 42]. Thus, the presence of a strong crystallographic texture with the prismatic direction aligned with the test axis could explain the anisotropic thermal expansion observed in this study for the temperature limits considered. However, texture in the α phase is not known to develop in the LPBF of Ti6Al4V [29]. Regarding the differences in microstructure between the three heat treatments to the thermal expansion results obtained, the lattice parameters of the α' and α phases are extremely close [80], therefore it follows that the martensitic α' which dominates the stress relieved microstructure and is present in the mill annealed microstructure should behave in a similar manner with respect to anisotropic thermal expansion. Instead, this may be attributable to the presence of β in the mill-annealed condition.

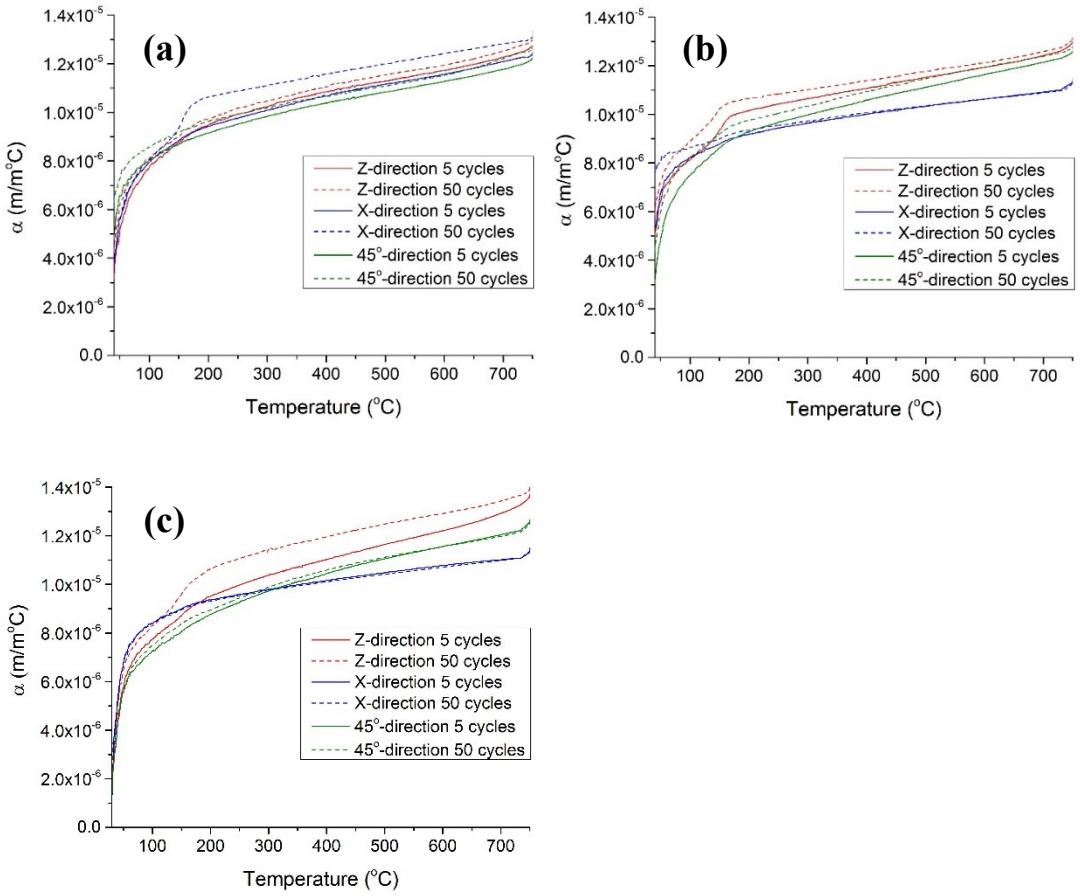

Figure 5-4: Comparative dilatometry curves after 5 and 50 cycles from ambient temperature to 750°C for samples in all three build directions following (a) stress relief, (b) mill annealing, and (c) HIP heat treatments.

Table 5-2: Average of linear CTE measurements at the 750°C plateau for the nine sample conditions over 50 cycles.

Avg CTE_{750C} ± s.d. over 50 cycles (x10^{-6} m/m°C)			
	Stress Relieved	**Mill Annealed**	**HIP**
Z-direction	12.9 ± 0.11	13.1 ± 0.11	13.8 ± 0.11
45°	12.6 ± 0.22	12.8 ± 0.12	12.6 ± 0.04
X-direction	12.8 ± 0.19	11.4 ± 0.04	11.4 ± 0.04

Previous studies have demonstrated the effects of heat treatment on various properties of LPBF fabricated Ti6Al4V samples which have been shown to yield objectively better or worse properties depending on the heat treatment chosen, and this is due to the resulting microstructure [13, 15, 73, 81]. Moreover, it has been suggested that the important microstructural changes induced by high-temperature heat treatments such as HIP processing may directly influence the thermal expansion coefficient in certain materials [82]. However in this case, the heat treatments selected appear to simply influence the degree of anisotropy causing the material to expand more or less depending on the build direction during fabrication. This is clear from the above results as the thermal expansions are shown to be statistically identical for all build directions in the stress-relieved condition, while mill annealing and HIP processing cause the thermal expansion coefficients to increase for samples built in the *Z-direction* and to decrease for samples built in the *X-direction*.

In terms of thermal stability however, the effects of the selected heat treatment are more easily quantified. Overall standard deviations were highest for the samples in the stress-relieved condition ($\pm 0.17 \times 10^{-6}$ compared with $\pm 0.09 \times 10^{-6}$ and $\pm 0.06 \times 10^{-6}$ for mill-annealed and HIP conditions respectively) suggesting poorer thermal stability following this heat treatment. Thermal stability is almost certainly influenced by the α' phase fraction. The martensitic transformation temperature T_m is known to occur at approximately 575 ^{o}C [79], well within the temperature ranges examined in the initial set of thermal cycles. Thus for an α' dominated microstructure, α'→α transformation may occur over this range and is therefore likely to be the least stable under these conditions, corresponding well with the reduced thermal stability for the stress-relieved specimens. This transformation is not instantaneous and would occur gradually during the thermal cycling process [83]. Parts in the HIP condition were shown to have the lowest overall standard deviations, indicating good thermal stability over 50 cycles. This is expected as the HIP heat treatment is

performed above the selected maximum temperature (750 ºC) for this set of thermal cycles reducing the possibility of changes to the microstructure during cycling.

From Figure 5-4, it is apparent that there is a noticeable difference between the CTE curves taken after 5 cycles and after 50 cycles. This is most apparent near 200 ºC, steadily declining as temperature increases, but is inconsistent between the samples and moreover appears to have very little impact if any on the final linear expansion measured at 750 ºC. Instead, a more representative measure of overall thermal stability over 50 cycles can be found by measuring the total increase or decrease in CTE at maximum temperature. An overall increase in linear thermal expansion values from 5 to 50 thermal cycles was measured at an average of 4.14% for stress relieved samples, 0.25% for mill annealed samples, and 0.88% for samples in the HIP condition. Thus, thermal stability was very high for samples in both the mill annealed and HIP conditions, while substantially lower in the stress relieved condition. Again, this is likely due to α'→α transformation occurring gradually in the stress relieved samples during thermal cycling [83].

Figure 5-5a shows the CTE evolution over the course of 50 cycles for a HIP sample built at 45º and cycled to a maximum temperature of 750 ºC, which behaved as expected. Figure 5-5b however shows an irregularity which was observed for a sample built in the *Z-direction*. In this instance, there is a noticeable inflection occurring between 150-200 ºC, resulting in a higher reported CTE at this temperature (Figure 5-5b). The inflection has been observed in a few other cases independent of build direction and heat treatment. This was observed to occur spontaneously after a number of cycles inconsistent between cases observed, ranging from the initial 10 cycles to the final 10 (Figure 5-6), suggesting defect evolution caused by the thermal cycling process. Once the inflection appears, it will remain throughout the remainder of the thermal cycles. On average, in samples where the inflection was present, this caused a sudden increase in CTE of approximately

$1.16x10^{-6}$ m/m°C, or roughly 12%, before gradually diminishing over the course of the heating cycle, causing very little effect on the expansion measured at maximum temperature.

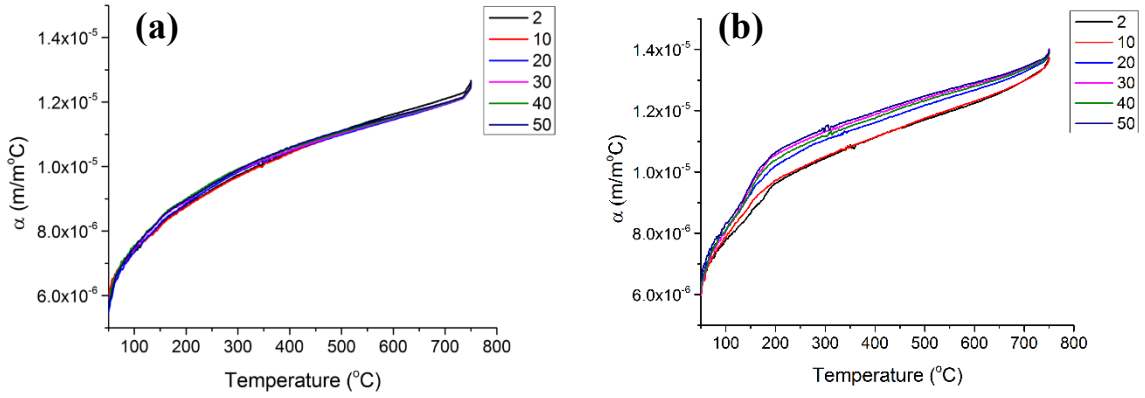

Figure 5-5: Coefficient of thermal expansion as a function of temperature and number of cycles for (a) a 45° built HIP sample, and (b) a z-direction HIP sample. Both samples were cycled 50 times from RT to 750°C.

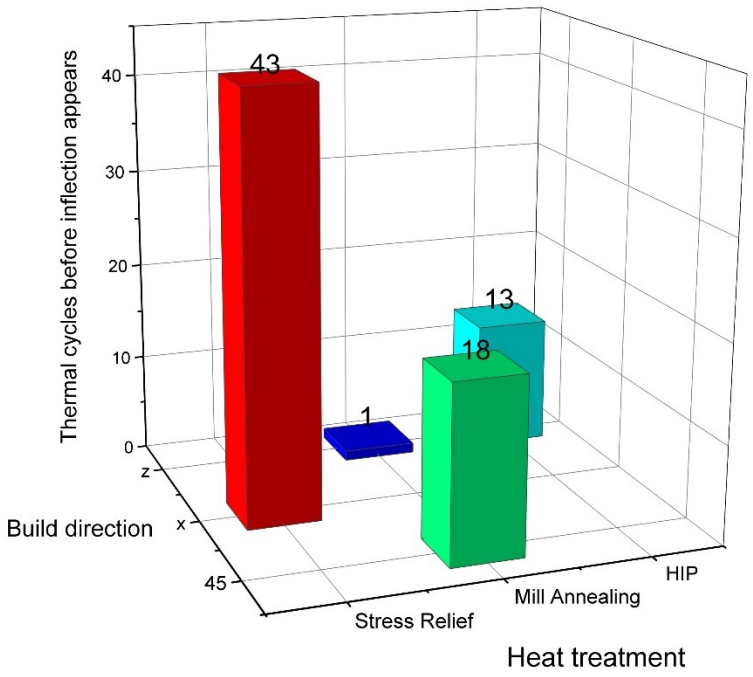

Figure 5-6: Number of thermal cycles before the appearance of an inflection in thermal expansion between 150 – 200°C, as a function of build direction and heat treatment applied.

Room temperature to 400 °C

A total of 6 tests were also performed from ambient temperature to 400 °C with identical heating rates, cooling rates, hold times, and number of cycles as with the initial set of thermal cycles. This

range of temperatures was chosen as it falls below the expected major microstructural transformation temperatures in Ti6Al4V [1, 84]. This range is below the holding temperatures for both the mill annealing and HIP heat treatments; therefore a better comparison of thermal stability can be made between samples treated in these two conditions. Dilatometry curves are presented in Figure 5-7 and average maximum linear CTE for the 6 samples tested under this regime are listed in Table 5-3. The anisotropic thermal expansion observed previously can be seen again in this set of experiments. CTE after 50 cycles from ambient temperature to 400 ^{o}C were measured at an average of $\alpha_X=11.2x10^{-6} \pm 0.02\ m/m^oC$, $\alpha_Z=12.0x10^{-6} \pm 0.46\ m/m^oC$ and $\alpha_{45}=11.3x10^{-6} \pm 0.02\ m/m^oC$ for the three mill annealed samples respectively and at an average of $\alpha_X=10.5x10^{-6} \pm 0.02\ m/m^oC$, $\alpha_Z=11.8x10^{-6} \pm 0.11\ m/m^oC$ and $\alpha_{45}=10.7x10^{-6} \pm 0.02\ m/m^oC$ for the three HIP samples respectively. The anisotropic thermal expansion is less pronounced over this range of temperatures and only becomes noticeable for the *Z-direction* samples above 300 ^{o}C, suggesting that the anisotropy is somehow restricted to high temperatures. The observation that the anisotropic expansion becomes significant past a certain temperature could be explained by the presence of β which has been shown to have much greater lattice expansion at higher temperatures [85-87]. As with the previous set of thermal cycles, the *Z-direction* samples showed the greatest thermal

expansion at maximum temperature. However, the difference between the *X-direction* and *45°* samples is very small in this case.

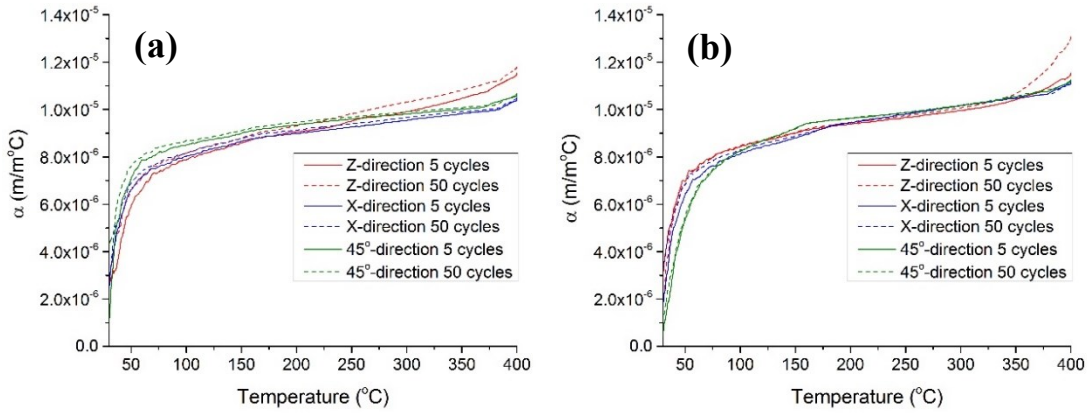

Figure 5-7: Comparative dilatometry curves from ambient temperature to 400°C after 5 and 50 cycles for all three build directions, following (a) HIP, and (b) mill annealing heat treatments.

Table 5-3: Average linear CTE measured at the 400°C plateau for six sample conditions.

Avg CTE_{400C} ± s.d. over 50 cycles (x10^{-6} m/m°C)		
	Mill Annealed	HIP
Z-direction	12.0 ± 0.46	11.8 ± 0.11
45°	11.3 ± 0.02	10.7 ± 0.02
X-direction	11.2 ± 0.02	10.5 ± 0.02

From Table 5-3, standard deviations are quite low at this temperature range indicating good thermal stability for both heat treatments, though as can be seen in Figure 5-7b, the *Z-direction* sample in the mill annealed condition suffered a gradual loss of stability as it neared the end of its 50 cycles indicating the possibility of a major defect in the sample as this effect was non-reproducible in any other observed condition. Because of this, the average standard deviations were quite high for the mill annealed samples at this temperature range (±0.17x10^{-6}), but is

otherwise extremely low for the two other samples considered. For the HIPed samples, even with the slightly higher than average standard deviation in the *Z-direction*, the average was measured at $\pm 0.05 \times 10^{-6}$ indicating excellent thermal stability.

5.3.7. Crystallographic texture and anisotropic thermal expansion

To determine whether the anisotropic thermal expansion observed in this study was due to the presence of a strong crystallographic texture, further analysis was required. Figure 5-8 presents thermal expansion data obtained from various literature sources for the basal and prismatic planes of the α-phase in Ti6Al4V [41, 42, 44, 45]. At low temperatures, expansion along the basal plane (*a*) of the hcp crystal appears to be more significant than along the prismatic plane (*c*), while at high temperatures the opposite is true showing behavior typical of hcp structures. While it is difficult to determine the theoretical inversion temperature from the limited high temperature data available in the literature, anisotropic thermal expansion will necessarily be less evident near the point at which inversion occurs and will become more pronounced as higher temperatures are reached. In the present study, thermal expansion anisotropy is shown to be most noticeable above 200-300 ºC.

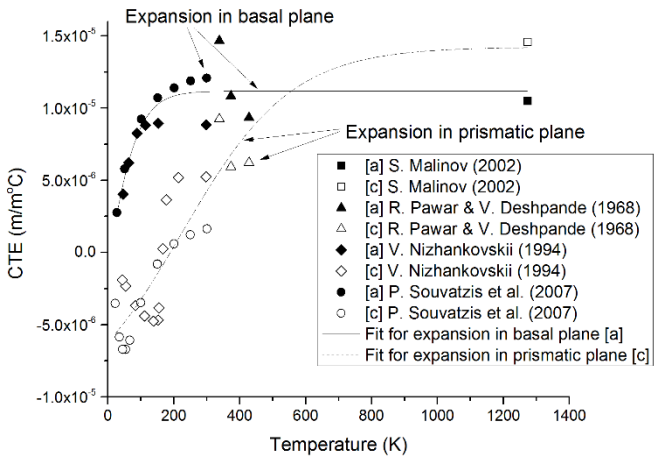

Figure 5-8: Literature values reported for the coefficient of thermal expansion of Ti6Al4V in the basal plane and the prismatic plane respectively, with an approximate fit showing a possible inversion point [41, 42, 44, 45].

EBSD has been performed on samples built in the *Z-direction* and in the *X-direction* and the results are shown in Figure 5-9, with IPF colouring normal to the plane of observation and showing the prior beta grains lengthwise along the test axis [15].

A visual inspection of the IPF orientation maps of the Ti-α phase suggest a random distribution in both the *Z-direction* and the *X-direction* samples. The pole figures generated from these maps and shown in Figure 5-10 support this claim, indicating very weak crystallographic texture if any. The {0001} pole figure shows some concentrations at several angles both perpendicularly and approximately parallel to the growth direction ultimately making it difficult to characterize. A random distribution in the α-phase would support previous work by M. Simonelli where EBSD of α-Ti was conducted on a similar LPBF built Ti6Al4V component [29]. Reconstructed β phase EBSD maps based on the maps obtained for the α phase are presented in Figure 5-11 and corresponding pole figures are shown in Figure 5-12. 'Variant selection' is known to occur during the β→α transformation of Ti6Al4V. In other words, based on the crystal orientation of a particular β grain, if variant selection occurs then a certain subgroup of the 12 possible α orientation variants will have an increased likelihood to be formed [88]. Thus, an overlying texture in the β phase may

have been indicative of less obvious trends in the crystal orientation of the α phase, due to the manner in which the β phase decomposes during solidification. Based on the reconstructed maps, there does not seem to be any clear crystallographic texture in the original β phase either, meaning that while preferential α orientations may appear within each individual prior-β grains, it cannot be inferred that a significant crystallographic texture in the α phase is present in the sample and thus it cannot be said from EBSD alone whether variant selection has occurred in this case or not.

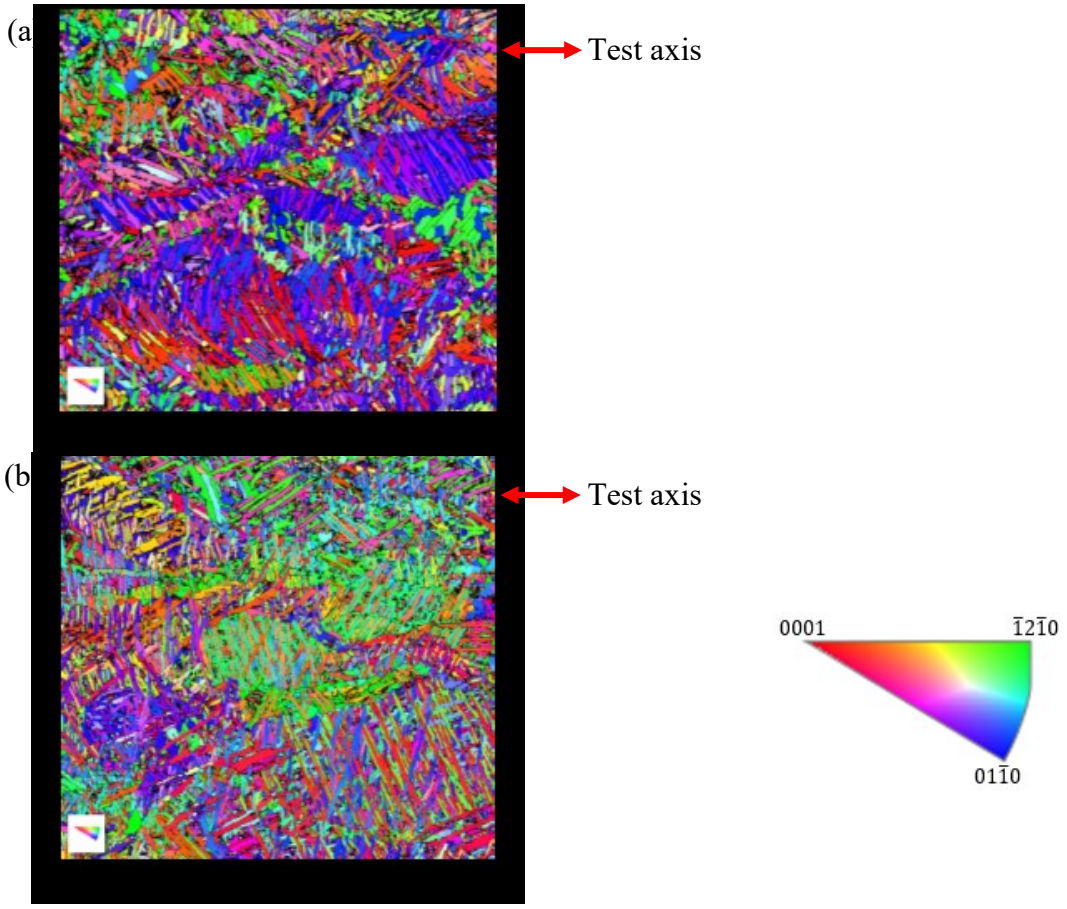

Figure 5-9: EBSD maps (IPF colouring normal to the plane of observation) of the α phase collected on (a) a cross sectional view of a sample built in the X-direction, and (b) a side view of a sample built in the Z-direction.

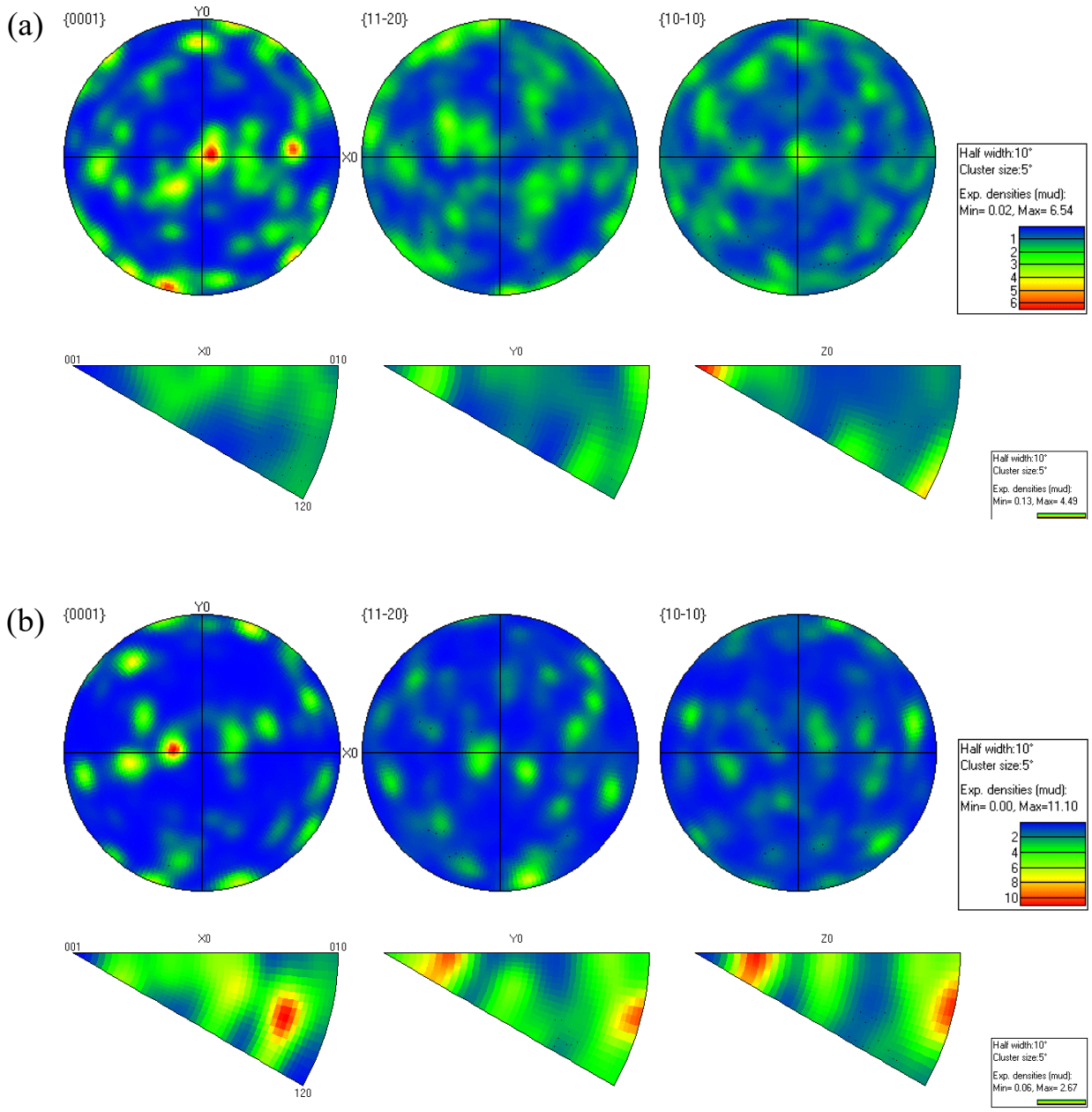

Figure 5-10: Pole figures and inverse pole figure depictions of the α-phase distribution for (a) a cross sectional view of a sample built in the X-direction, and (b) a side view of a sample built in the Z-direction.

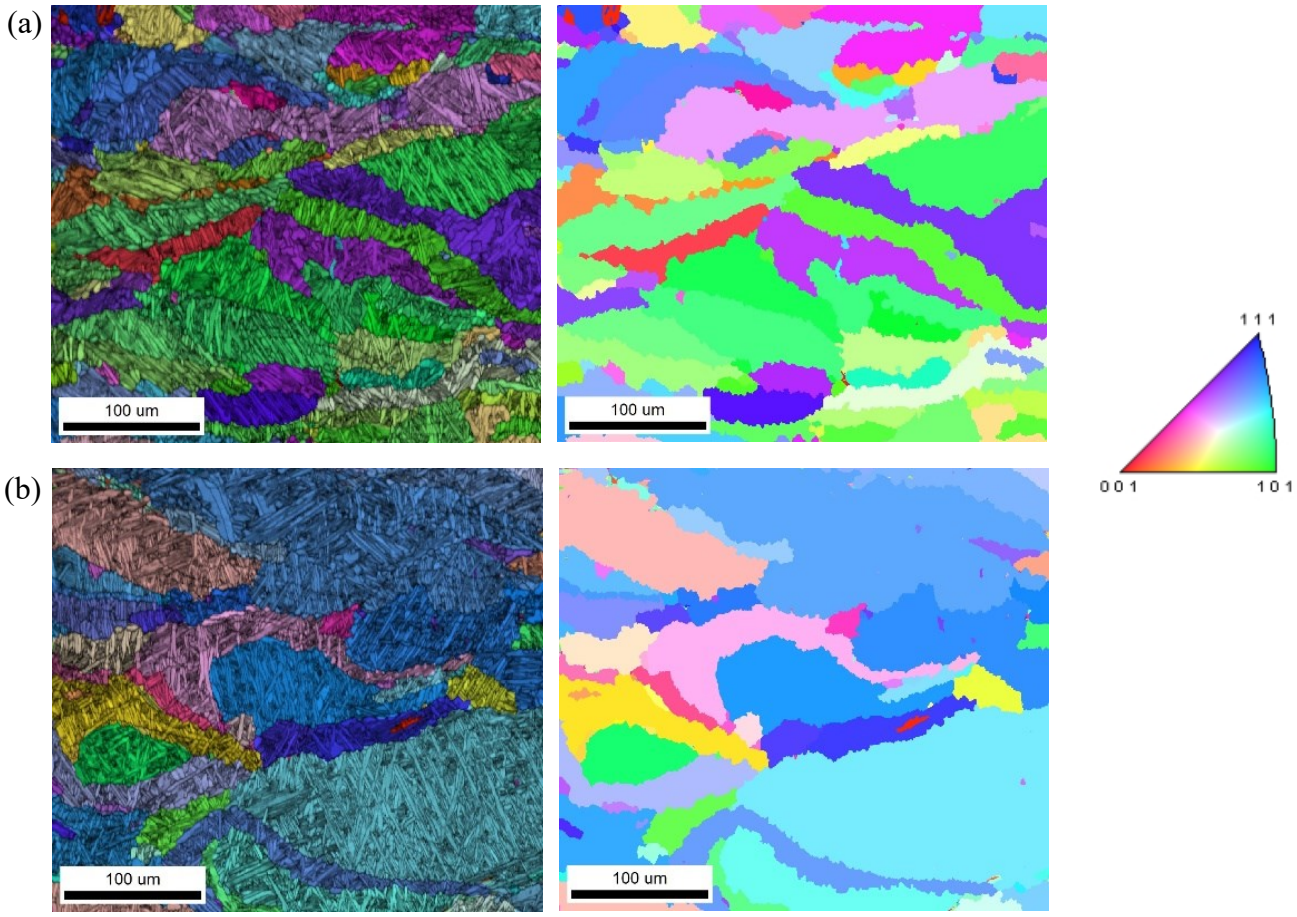

Figure 5-11: Reconstructed β phase EBSD maps (IPF Z colouring) for (a) a side view of a sample built in the X-direction and (b) a cross sectional view of a sample built in the Z-direction.

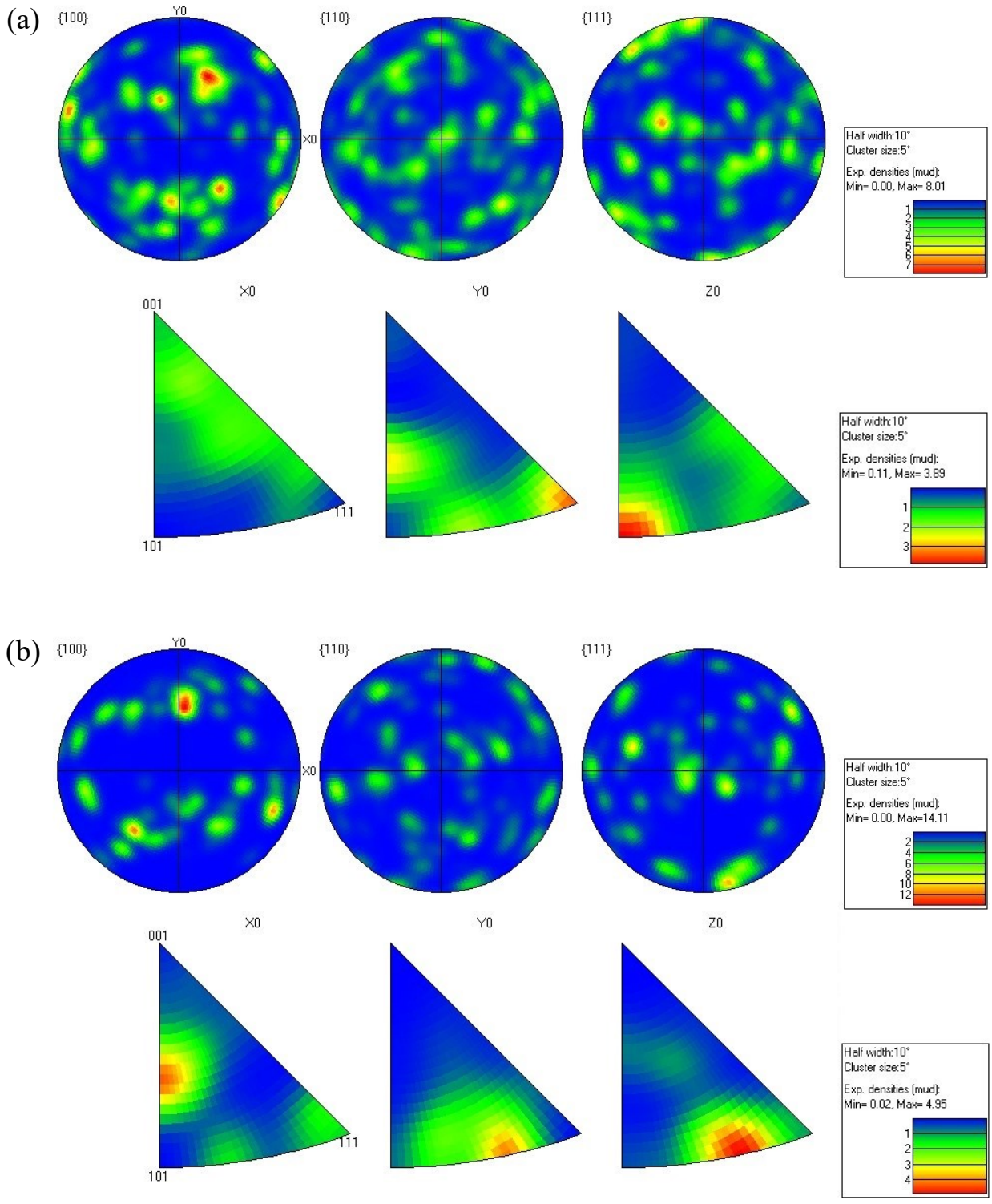

Figure 5-12: Pole figures and inverse pole figure depictions of the reconstructed β-phase for (a) a cross sectional view of a sample built in the X-direction, and (b) a side view of a sample built in the Z-direction.

Interestingly, the results obtained in this study show close similarities to results obtained by Z. Li et al. [89]. In their study, very similar anisotropic bulk thermal expansion characteristics were observed in TC21, another α-β titanium alloy, produced through powder deposition AM. From their experiments, macro-scale thermal expansion in the longitudinal direction (i.e. along the growth direction) was found to be greater than in other directions in the range of ~580 – 1000 ºC for samples containing both the α and β phase, while the thermal expansion was nearly identical for all build directions at lower temperatures. EBSD was performed on a larger area and corresponding pole figures had suggested that the c-axis {0001} of the Ti-α had a slight tendency to be oriented perpendicularly to the build direction, while $\{11\bar{2}0\}$ was difficult to identify due to symmetry. The orientation of the basal plane appears to directly contradict the expected thermal expansion according to single crystal Ti-α lattice expansion as shown in Figure 5-8 as literature suggests expansion should be greater along the basal direction at higher temperatures. Instead, it was suggested that anisotropic expansion of the lattice during α→β phase transformation coupled with a similar anisotropy at the macro level could be a strong yet less easily identifiable indication that variant selection has taken place. Lattice parameters were determined through XRD and differences in d-spacing between the α and β phases were quantified. It was determined that contraction of the d-spacing by -4.18% and -1.85% occurred along the $[1\bar{1}1]\beta//[11\bar{2}0]\alpha$ and $[011]\beta//[0001]\alpha$ (denoted d_1 and d_3) directions respectively while expansion of 4.31% occurred along the $[21\bar{1}]\beta//[1\bar{1}00]\alpha$ (denoted d_2) direction confirming lattice expansion anisotropy during phase transformation and corresponding well with the high temperature (>1000 ºC) bulk thermal expansions obtained [89].

From our own XRD analysis, very similar α→β lattice expansion characteristics were obtained for a HIP specimen. Lattice parameters, d-spacings, and expansions in the lattice space were

calculated and are shown in Table 5-4. This as well as the fact that the thermal expansion of the HIP samples in this study behaved extremely similarly to the α-β TC21 studied by Z. Li et al. [89] up to 750 ºC suggests very strong similarities between these two samples both at the micro and macro level. Thus it can be said with fair confidence that variant selection has occurred, despite inconclusive EBSD results. It is difficult to perform this same analysis on the stress-relieved and mill-annealed specimens however, as the β phase was either absent or its volume fraction was too low to determine its lattice parameters.

Table 5-4: From XRD, measured lattice parameter and d-spacings in the α and β phases along with calculated expansion occurring during α->β transformation.

		d_1	d_2	d_3
α (a=2.94, c=4.68)		2.94 Å	2.54 Å	2.32 Å
β (c=3.23)		2.80 Å	2.64 Å	2.28 Å
% difference	**This study**	**-4.76%**	**3.69%**	**-2.56%**
	Z. Li et al. [89]	-4.18%	4.41%	-2.34%

5.3.8.Residual stress measurements

Three dilatometer test samples were measured for residual stresses: (1) an uncycled stress relieved sample, (2), an initially stress relieved sample subjected to 50 cycles following the high temperature thermal cycling regime discussed above (RT to 750ºC), and (3) an identical sample subjected to the same thermal cycling schedule followed by a stress relief heat treatment. Results for the three samples are presented in Table 5-5.

Table 5-5: Residual stress measurements by XRD for three dilatometer samples.

	Uncycled	50 cycles	50 cycles + SR
σ_{11} (MPa)	-3.26 ± 45.83	15.34 ± 46.00	-47.83 ± 39.58
σ_{22} (MPa)	-1.79 ± 35.80	-33.72 ± 35.61	-8.98 ± 31.04

The results shown above demonstrate that the thermal cycling regime tested in this study represents a statistically insignificant source of residual stresses, as expected. The heating and cooling rates employed during thermal cycling are far below those experienced during LPBF processing, and slow enough that any residual stresses arising from said heating or cooling cycles are relieved when the sample is held at each high temperature plateau.

5.4. Conclusions

A series of dilatometry experiments were performed on Ti6Al4V samples fabricated by LPBF with varying processing and post-processing conditions and the following observations were made:

- Anisotropic linear thermal expansion was observed depending on the build direction of the specimen during LPBF. Samples built in the *z*-direction exhibited the greatest thermal expansion while samples built in the *x*-direction exhibited the lowest thermal expansion. The HCP Ti-α phase has been shown in previous studies to have anisotropic lattice expansion, thus crystallographic texture was examined. However, no strong texture in the α phase was observed by EBSD. A comparison with a recent study on a similar alloy has suggested that despite this, anisotropic lattice expansion during the α→β transformation could be indicative that variant selection has occurred [89]. Through XRD, d-spacings expansions and contractions in the HIP specimen were found to be strikingly similar to

those measured by Z. Li et al., suggesting that variant selection is extremely likely in this case as well.

- HIP was expected to provide the greatest thermal stability as the heat treatment is performed at the highest temperature of the three treatments chosen, yet still falls below the β-transus temperature. From the high temperature cycling (RT to 750 ºC), comparing the three heat treatments indicates that both HIP and mill annealing yielded excellent thermal stability, with slightly lower overall standard deviations reported for the HIP samples, while stress relieved samples showed the poorest thermal stability. The poorer thermal stability in the stress relieved sample is almost certainly due to the martensitic microstructure obtained following this heat treatment.
- Thermal cycling was shown to be an insignificant source of residual stresses in the cases discussed in this study. Any onset of residual stresses due to the elevated rate of heating/cooling is most likely relieved when the maximum temperature is maintained.

5.5. Acknowledgements

The authors acknowledge PWC for supplying temperature range, heating rate, and cooling rate for thermal cycling. The authors also acknowledge CRIAQ and industrial sponsors GE Aviation, Bell Helicopter, MDA, Héroux Devtek, CMQ, CLS, Bombardier Aerospace, Liburdi, and Edmit Industries for support.

Chapter 6 – Summary

The objective of the current work was to analyse the various thermal response characteristics of Ti6Al4V during and following fabrication by LPBF, namely distortions due to process-induced thermal stresses and thermal expansion based on certain process and design variables. With this information, a better understanding on LPBF as a viable industrial process for this alloy can be obtained. In-depth experimental work and analysis was performed yielding interesting results. A summary of the results from Chapters 4 and 5 is presented as follows.

- Thermal stresses were shown to exceed the yield strength of the material which led to significant distortions in sample geometry. Certain design factors were shown to directly influence the magnitude of deformations. The tube wall thickness non-linearly affected the magnitude of deformations with greatest distortions recorded for the thinnest walled samples. Increasing the specimen length leads to increasing deformations, though the trend appears to plateau at greater lengths. The angle of overhang was a more complex variable; a lower angle to the horizontal, and thus a more uniform cross section, was shown to reduce the magnitude of deformations compared with a higher angle to the horizontal and thus a cross section with an elevated aspect ratio.
- Stress relieved samples showed little to no deformations following separation from the base plate, confirming the heat treatment selected. On untreated samples, further deformations were recorded following separation due to relaxation effects. In one case, relaxation was so severe that the part suffered catastrophic failure. Greater deformation during relaxation was observed for the sample with the greatest wall thickness. Surface residual stress measurements support this observation.

- The coefficient of thermal expansion (CTE) of Ti6Al4V fabricated by LPBF is highly dependent on the build direction. In general, samples built in the *z*-direction showed greater thermal expansion than samples build in the *x*-direction. Samples built at 45° showed a thermal expansion between *z*- and *x*-directions. Crystallographic texture was studied and though a random distribution was obtained through EBSD, lattice expansion measurements from $\alpha \rightarrow \beta$ transformation support the findings in a previous study where similar anisotropic expansion was observed, strongly suggesting that variant selection did occur in the α phase.
- The dependence on build direction described above was itself affected by the heat treatment applied. Stress relieved specimens showed statistically no difference in thermal expansion with build direction, whereas annealing and HIP processing both yielded this phenomenon.
- The thermal stability of the material when exposed to thermal cycling was highest for HIP and mill annealed specimens and lowest for stress relieved specimens when cycled from 25 – 750 °C. At lower temperature (25 – 400 °C), thermal stability was similarly equivalent for HIP and mill annealing conditions.
- Thermal cycling was not shown to generate significant residual stresses under the conditions examined in the present work which roughly approximate aerospace engine conditions.

Chapter 7 – Bibliography

[1] M. J. Donachie, *Titanium: A Technical Guide, 2nd Edition*. ASM International, 2000.

[2] B. Vandenbroucke and J. P. Kruth, "Selective laser melting of biocompatible metals for rapid manufacturing of medical parts," *Rapid Prototyping Journal,* vol. 13, no. 4, pp. 196-203, 2007.

[3] M. Peters, J. Kumpfert, C. H. Ward, and C. Leyens, "Titanium Alloys for Aerospace Applications," Titanium and Titanium Alloys: Fundamentals and Applications, C. Leyens and M. Peters, Eds., Online: Wiley-VCH Verlag GmbH & Co. KGaA, 2003, pp. 333-350. [Online]. Available.

[4] T. Wohlers and T. Gornet, "History of additive manufacturing," *Wohlers Report,* vol. 24, p. 2014, 2014.

[5] J. Kruth, "Material increase manufacturing by rapid prototyping technique," *Annals of the CIPP,* vol. 40, no. 2, pp. 603-604, 1999.

[6] P. F. Jacobs, D. T. Reid, Computer, and A. S. A. o. SME., *Rapid Prototyping & Manufacturing: Fundamentals of Stereolithography*. Society of Manufacturing Engineers, 1992.

[7] B. Baufeld, E. Brandl, and O. Van der Biest, "Wire based additive layer manufacturing: comparison of microstructure and mechanical properties of Ti–6Al–4V components fabricated by laser-beam deposition and shaped metal deposition," *Journal of Materials Processing Technology,* vol. 211, no. 6, pp. 1146-1158, 2011.

[8] M. L. Griffith *et al.*, "Understanding thermal behavior in the LENS process," *Materials & Design,* vol. 20, no. 2–3, pp. 107-113, 6/1/ 1999.

[9] E. C. Santos, M. Shiomi, K. Osakada, and T. Laoui, "Rapid manufacturing of metal components by laser forming," *International Journal of Machine Tools and Manufacture,* vol. 46, no. 12–13, pp. 1459-1468, 10// 2006.

[10] P. Mercelis and J. P. Kruth, "Residual stresses in selective laser sintering and selective laser melting," *Rapid Prototyping Journal,* vol. 12, no. 5, pp. 254-265, 2006/10/01 2006.

[11] J. Delgado, J. Ciurana, and C. Rodríguez, "Influence of process parameters on part quality and mechanical properties for DMLS and SLM with iron-based materials," (in English), *The International Journal of Advanced Manufacturing Technology,* vol. 60, no. 5-8, pp. 601-610, 2012/05/01 2012.

[12] B. Song, S. Dong, Q. Liu, H. Liao, and C. Coddet, "Vacuum heat treatment of iron parts produced by selective laser melting: Microstructure, residual stress and tensile behavior," *Materials & Design,* vol. 54, no. 0, pp. 727-733, 2// 2014.

[13] S. Leuders *et al.*, "On the mechanical behaviour of titanium alloy TiAl6V4 manufactured by selective laser melting: Fatigue resistance and crack growth performance," *International Journal of Fatigue,* vol. 48, no. 0, pp. 300-307, 3// 2013.

[14] R. Chou, J. Milligan, M. Paliwal, and M. Brochu, "Additive Manufacturing of Al-12Si Alloy Via Pulsed Selective Laser Melting," *JOM,* vol. 67, no. 3, pp. 590-596, 2015// 2015.

[15] J. Mezzetta, "Process-Property Relationships of Ti6Al4V Fabricated through Selective Laser Melting," Master of Engineering, Department of Mining and Materials Engineering, McGill University, Montreal, QC, 2016.

[16] M. S. Abdul Aziz *et al.*, "Residual Stress and Deformation of Consolidated Structure Obtained by Layered Manufacturing Process," *Journal of Advanced Mechanical Design, Systems, and Manufacturing,* vol. 7, no. 2, pp. 244-256, 2013.
[17] M. Zaeh and G. Branner, "Investigations on residual stresses and deformations in selective laser melting," (in English), *Production Engineering,* vol. 4, no. 1, pp. 35-45, 2010/02/01 2010.
[18] L. E. Murr *et al.*, "Microstructure and mechanical behavior of Ti–6Al–4V produced by rapid-layer manufacturing, for biomedical applications," *Journal of the Mechanical Behavior of Biomedical Materials,* vol. 2, no. 1, pp. 20-32, 1// 2009.
[19] M. Shiomi, K. Osakada, K. Nakamura, T. Yamashita, and F. Abe, "Residual Stress within Metallic Model Made by Selective Laser Melting Process," *CIRP Annals - Manufacturing Technology,* vol. 53, no. 1, pp. 195-198, 2004/01/01 2004.
[20] M. A. Khan, R. L. Williams, and D. F. Williams, "The corrosion behaviour of Ti–6Al–4V, Ti–6Al–7Nb and Ti–13Nb–13Zr in protein solutions," *Biomaterials,* vol. 20, no. 7, pp. 631-637, 1999/04/01 1999.
[21] F. A. Kandil, J. D. Lord, A. T. Fry, and P. V. Grant, "A review of residual stress measurement methods - a guide to technique selection," National Physical Laboratory2001, vol. NPL Report MATC(A)04.
[22] M. E. Fitzpatrick and N. P. Laboratory, *Determination of Residual Stresses by X-ray Diffraction* (no. no. 2). National Physical Laboratory, 2005.
[23] P. Rangaswamy *et al.*, "Residual stresses in LENS® components using neutron diffraction and contour method," *Materials Science and Engineering: A,* vol. 399, no. 1–2, pp. 72-83, 6/15/ 2005.
[24] T. A. Krol, C. Seidel, J. Schilp, M. Hofmann, W. Gan, and M. F. Zaeh, "Verification of structural simulation results of metal-based additive manufacturing by means of neutron diffraction," *Physics Procedia,* vol. 41, pp. 849-857, 2013.
[25] X. Song *et al.*, "Residual stresses and microstructure in Powder Bed Direct Laser Deposition (PB DLD) samples," (in English), *International Journal of Material Forming,* pp. 1-10, 2014/01/21 2014.
[26] C. R. Knowles, T. H. Becker, and R. B. Tait, "Residual stress measurements and structural integrity implications for selective laser melted TI-6Al-4V," *South African Journal of Industrial Engineering,* vol. 23, no. 3, pp. 119-129, 2012.
[27] H. Attar, M. Calin, L. C. Zhang, S. Scudino, and J. Eckert, "Manufacture by selective laser melting and mechanical behavior of commercially pure titanium," *Materials Science and Engineering: A,* vol. 593, pp. 170-177, 1/21/ 2014.
[28] T. Furumoto, T. Ueda, M. S. Abdul Aziz, A. Hosokawa, and R. Tanaka, "Study on reduction of residual stress induced during rapid tooling process: Influence of heating conditions on residual stress," *Key Engineering Materials,* vol. 447-448, pp. 785-789, 2010.
[29] M. Simonelli, Y. Y. Tse, and C. Tuck, "On the Texture Formation of Selective Laser Melted Ti-6Al-4V," *Metallurgical and Materials Transactions A,* vol. 45, no. 6, pp. 2863-2872, 2014// 2014.
[30] H.-S. Byun and K. H. Lee, "Determination of the optimal build direction for different rapid prototyping processes using multi-criterion decision making," *Robotics and Computer-Integrated Manufacturing,* vol. 22, no. 1, pp. 69-80, 2// 2006.

[31] T. A. Krol, M. F. Zaeh, J. Schilp, and C. Seidel, "Computational-efficient designs of support structures and material modeling for metal-based additive manufacturing," in *CADFEM (Hg.): ANSYS Conference and 29th CADFEM Users' Meeting 2011*, 2011.

[32] T. A. Krol, M. F. Zaeh, and C. Seidel, "Optimization of supports in metal-based additive manufacturing by means of finite element models," in *22. Solid Freeform Fabrication Conference*, 2012.

[33] J. E. Muelaner, O. Martin, and P. Maropoulos, "Metrology Enhanced Tooling for Aerospace (META): Strategies for Improved Accuracy of Jig Built Structures," 2011. Available: http://dx.doi.org/10.4271/2011-01-2557

[34] P. Homporova, C. Poletti, M. Stockinger, and F. Warchomicka, "Dynamic phase evolution in titanium alloy Ti-6A1-4V," in *12th World Conference on Titanium, Ti 2011, June 19, 2011 - June 24, 2011*, Beijing, China, 2012, vol. 1, pp. 737-740: Science Press.

[35] K. Mutombo, S. Charles, and W. Stumpf, "Phase Transformation Cycle [beta][arrow right] [alpha]' + [alpha] + [alpha]"[arrow right] [beta] in Ti6Al4V Alloy," (in English), *Materials Science Forum,* vol. 828-829, pp. 232-238, Aug 2015.

[36] P. Tarin, A. Gualo, A. G. Simon, N. M. Piris, and J. M. Badia, "Study of alpha-beta transformation in Ti-6Al-4V-ELI. Mechanical and microstructural characteristics," in *6th International Conference on Processing and Manufacturing of Advanced Materials - THERMEC'2009, August 25, 2009 - August 29, 2009*, Berlin, Germany, 2010, vol. 638-642, pp. 712-717: Trans Tech Publications Ltd.

[37] A. Bhattacharjee, S. B., and J. C. Williams, "Titanium Alloys: Part 2 - Alloy Development, Properties and Applications," in *Aerospace Materials and Material Technologies: Volume 1: Aerospace Materials*, N. E. Prasad and R. J. H. Wanhill, Eds.: Springer Singapore, 2016, pp. 117-148.

[38] A. P. Mouritz, "Titanium alloys for aerospace structures and engines A2," in *Introduction to Aerospace Materials*, A. P. Mouritz, Ed.: Woodhead Publishing, 2012, pp. 202-223.

[39] M. J. R. Barboza *et al.*, "Creep behavior of Ti–6Al–4V and a comparison with titanium matrix composites," *Materials Science and Engineering: A,* vol. 428, no. 1–2, pp. 319-326, 7/25/ 2006.

[40] L. Badea, M. Surand, J. Ruau, and B. Viguier, "Creep behavior of Ti-6Al-4V from 450° C to 600° C," *University Polytechnica of Bucharest Scientific Bulletin, Series B,* vol. 76, no. 1, pp. 185-196, 2014.

[41] V. I. Nizhankosvkii, M. I. Katsnel'son, G. V. Peschanskikh, and A. V. Trefilov, "Anisotropy of the thermal expansion of titanium due to proximity to an electronic topological transition," *Soviet Journal of Experimental and Theoretical Physics Letters,* vol. 59, p. 733, 1994.

[42] P. Souvatzis, O. Eriksson, and M. I. Katsnelson, "Anomalous Thermal Expansion in $\ensuremath{\alpha}$-Titanium," *Physical Review Letters,* vol. 99, no. 1, p. 015901, 07/06/ 2007.

[43] A. Shiro, M. Nishida, T. Hanabusa, and T. Jing, "Residual stress estimation of Ti casting alloy by x-ray single crystal measurement method," *International Centre for Diffraction Data,* vol. 52, pp. 413-420, 2009.

[44] R. R. Pawar and V. T. Deshpande, "The anisotropy of the thermal expansion of [alpha]-titanium," *Acta Crystallographica Section A,* vol. 24, no. 2, pp. 316-317, 1968.

[45] S. Malinov, W. Sha, Z. Guo, C. C. Tang, and A. Long, "Synchrotron X-ray diffraction study of the phase transformations in titanium alloys," *Materials Characterization,* Article vol. 48, no. 4, pp. 279-295, 6 2002.

[46] S. Manikandan and S. Ramanathan, "FLOW BEHAVIOUR OF THERMAL CYCLED TITANIUM (Ti-6Al-4V) ALLOY," *International Journal of Mechanical Engineering and Robotics Research,* vol. 2, no. 2, pp. 20-32, April 2013 2013.
[47] S. Manikandan, S. Ramanathan, and V. Ramakrishnan, "A Calorimetric Study of Ti-6AL-4V Alloy," *Indian Journal of Science and Technology,* Thermal Analysis, Differential Scanning Calorimeter, Specific Heat, Heat Treatment 2013.
[48] P. Lv *et al.*, "Effect of thermocycling on the microstructure of Ti-6Al-4V alloy in simulated low Earth orbit space environment," *Science China Materials,* vol. 59, no. 5, pp. 363-370, 2016// 2016.
[49] I. Palchan, "The transition effect in the cyclic temperature creep of Ti-6Al-4V," *Material Science and Engineering,* vol. 43, no. 3, pp. 217-23, 05/ 1980.
[50] M. N. Mungole, R. Kanojiya, R. Sharma, and B. Panda, "Thermal cycling In (α+β) Ti6Al4V alloy," *Transactions of the Indian Institute of Metals,* journal article vol. 61, no. 2, pp. 93-97, 2008.
[51] E. Amsterdam, "Evaluation of the microstructure and mechanical properties of laser additive manufactured gas turbine alloys Ti-6Al-4V and Inconel 718 [NLR-TP-2009-656]," (in English), *NLR Technical Reports,* pp. 1-25, 2009 2009.
[52] G. Branner, *Modellierung transienter Effekte in der Strukturs*imulation *von Schichtbauverfahren*. Utz, 2011.
[53] D. Thomas and R. Bibb, "Identifying the geometric constraints and process specific challenges of selective laser melting," in *Time Compression Technologies Rapid Manufacturing Conference*, Conventry, UK, 2008.
[54] A. Hussein, L. Hao, C. Yan, R. Everson, and P. Young, "Advanced lattice support structures for metal additive manufacturing," *Journal of Materials Processing Technology,* vol. 213, no. 7, pp. 1019-1026, 7// 2013.
[55] T. Mukherjee, J. S. Zuback, A. De, and T. DebRoy, "Printability of alloys for additive manufacturing," *Scientific Reports,* Article vol. 6, p. 19717, 01/22/online 2016.
[56] *Heat Treatment of Titanium Alloy Parts*, 2014.
[57] A. S. Wu, D. W. Brown, M. Kumar, G. F. Gallegos, and W. E. King, "An Experimental Investigation into Additive Manufacturing-Induced Residual Stresses in 316L Stainless Steel," *Metallurgical and Materials Transactions A,* vol. 45, no. 13, pp. 6260-6270, 2014/12/01 2014.
[58] I. Yadroitsava and I. Yadroitsev, "Residual Stress in Metal Specimens Produced by Direct Metal Laser Sintering," presented at the Annual International Solid Freeform Fabrication Symposium, 2015.
[59] H. Pohl, A. Simchi, M. Issa, and H. Calefi Dias, "Thermal Stresses in Direct Metal Laser Sintering," in *Solid Freeform Fabrication Simposium*, 2001, pp. 366-372.
[60] J.-P. Kruth, J. Deckers, E. Yasa, and R. Wauthlé, "Assessing and comparing influencing factors of residual stresses in selective laser melting using a novel analysis method," *Proceedings of the Institution of Mechanical Engineers, Part B: Journal of Engineering Manufacture,* vol. 226, no. 6, pp. 980-991, 2012/06/01 2012.
[61] A. E. Patterson, S. L. Messimer, and P. A. Farrington, "Overhanging Features and the SLM/DMLS Residual Stresses Problem: Review and Future Research Need," *Technologies,* vol. 5, no. 2, 2017.

[62] D. Wang, Y. Yang, Z. Yi, and X. Su, "Research on the fabricating quality optimization of the overhanging surface in SLM process," *The International Journal of Advanced Manufacturing Technology,* vol. 65, no. 9, pp. 1471-1484, 2013/04/01 2013.
[63] S. Timoshenko, "Analysis of Bi-Metal Thermostats," *Journal of the Optical Society of America,* vol. 11, no. 3, pp. 233-255, 1925/09/01 1925.
[64] C. Amon *et al.*, "Material Issues in Layered Forming," in *1993 Solid Freeform Fabrication Symposium*, 1993.
[65] K. Dai and L. Shaw, "Finite element analysis of the effect of volume shrinkage during laser densification," *Acta Materialia,* vol. 53, no. 18, pp. 4743-4754, 2005/10/01/ 2005.
[66] J. P. Kruth, P. Mercelis, J. Van Vaerenbergh, and T. Craeghs, "Feedback control of selective laser melting," presented at the 3rd International Conference on Advanced Research in Virtual and Rapid Prototyping Leiria, Portugal, 2007.
[67] A. V. Gusarov and E. P. Kovalev, "Model of thermal conductivity in powder beds," *Physical Review B,* vol. 80, no. 2, p. 024202, 07/07/ 2009.
[68] Y. Li and D. Gu, "Thermal behavior during selective laser melting of commercially pure titanium powder: Numerical simulation and experimental study," *Additive Manufacturing,* vol. 1, pp. 99-109, 2014/10/01/ 2014.
[69] T.-M. Wang, J.-T. Xi, and Y. Jin, "A model research for prototype warp deformation in the FDM process," *The International Journal of Advanced Manufacturing Technology,* vol. 33, no. 11, pp. 1087-1096, 2007/08/01 2007.
[70] Z. Zhu, V. Dhokia, A. Nassehi, and S. T. Newman, "Investigation of part distortions as a result of hybrid manufacturing," *Robotics and Computer-Integrated Manufacturing,* vol. 37, pp. 23-32, 2016/02/01/ 2016.
[71] M. Cloots, L. Zumofen, A. B. Spierings, A. Kirchheim, and K. Wegener, "Approaches to minimize overhang angles of SLM parts," *Rapid Prototyping Journal,* vol. 23, no. 2, pp. 362-369, 2017/03/20 2017.
[72] S. Heimann, M. Pohl, A. M. Klaska, and T. Beck, "Residual stress development due to thermal cycling of the particle-reinforced alloy EN AW-6061– experiment and simulation," *International Journal of Materials Research,* vol. 97, no. 12, pp. 1627-1632, 2006/12/01 2006.
[73] M. Simonelli, Y. Y. Tse, and C. Tuck, "Effect of the build orientation on the mechanical properties and fracture modes of SLM Ti–6Al–4V," *Materials Science and Engineering: A,* vol. 616, pp. 1-11, 2014/10/20/ 2014.
[74] K. Farmanesh and A. Najafi-Zadeh, "Thermomechanical behavior of Ti-6Al-4V alloy," *Journal of Materials Science and Technology,* vol. 19, no. 3, pp. 217-220, 2003.
[75] *Standard Specification for Additive Manufacturing Titanium-6 Aluminum-4 Vanadium with Powder Bed Fusion*, 2014.
[76] W. Case. (1994). *Explanation of the Coefficient of Thermal Expansion (CTE) for Use in NASTRAN*.
[77] P. A. Kobryn and S. L. Semiatin, "Microstructure and texture evolution during solidification processing of Ti–6Al–4V," *Journal of Materials Processing Technology,* vol. 135, no. 2–3, pp. 330-339, 4/20/ 2003.
[78] L. Thijs, F. Verhaeghe, T. Craeghs, J. V. Humbeeck, and J.-P. Kruth, "A study of the microstructural evolution during selective laser melting of Ti–6Al–4V," *Acta Materialia,* vol. 58, no. 9, pp. 3303-3312, 5// 2010.

[79] W. Xu *et al.*, "Additive manufacturing of strong and ductile Ti-6Al-4V by selective laser melting via in sity martensite decomposition," *Acta Materialia,* vol. 85, pp. 74-84, 2015.
[80] X. Tan *et al.*, "Revealing martensitic transformation and α/β interface evolution in electron beam melting three-dimensional-printed Ti-6Al-4V," *Scientific Reports,* vol. 6, p. 26039, 2016.
[81] B. Vrancken, L. Thijs, J.-P. Kruth, and J. Van Humbeeck, "Heat treatment of Ti6Al4V produced by Selective Laser Melting: Microstructure and mechanical properties," *Journal of Alloys and Compounds,* vol. 541, pp. 177-185, 2012.
[82] M. Yu-quan, "Effect of High Pressure Heat Treatment on Microstructure and Thermal Expansion Coefficients of Cu–Al Alloy," *MATERIALS TRANSACTIONS,* vol. 54, no. 4, pp. 540-543, 2013.
[83] J. I. Qazi, O. N. Senkov, J. Rahim, and F. H. Froes, "Kinetics of martensite decomposition in Ti–6Al–4V–xH alloys," *Materials Science and Engineering: A,* vol. 359, no. 1, pp. 137-149, 2003/10/25/ 2003.
[84] P. Tarin *et al.*, "Structural transformations in Ti-6Al-4V alloy," in *IIIrd European Symposium on Martensitic Transformations. ESOMAT'94, 14-16 Sept. 1994*, France, 1995, vol. 5, pp. 317-24.
[85] J. W. Elmer, T. A. Palmer, S. S. Babu, and E. D. Specht, "In situ observations of lattice expansion and transformation rates of α and β phases in Ti–6Al–4V," *Materials Science and Engineering: A,* vol. 391, no. 1, pp. 104-113, 2005/01/25/ 2005.
[86] A. K. Swarnakar, O. Van der Biest, and B. Baufeld, "Thermal expansion and lattice parameters of shaped metal deposited Ti–6Al–4V," *Journal of Alloys and Compounds,* vol. 509, no. 6, pp. 2723-2728, 2011/02/10/ 2011.
[87] R. Pederson, O. Babushkin, F. Skystedt, and R. Warren, "Use of high temperature X-ray diffractometry to study phase transitions and thermal expansion properties in Ti-6Al-4V," *Materials Science and Technology,* vol. 19, no. 11, pp. 1533-1538, 2003/11/01 2003.
[88] N. Stanford and P. S. Bate, "Crystallographic variant selection in Ti–6Al–4V," *Acta Materialia,* vol. 52, no. 17, pp. 5215-5224, 10/4/ 2004.
[89] Z. Li, J. Li, Y. Zhu, X. Tian, and H. Wang, "Variant selection in laser melting deposited α + β titanium alloy," *Journal of Alloys and Compounds,* vol. 661, no. Complete, pp. 126-135, 2016.